UNIVERSITY OF CALIFORNIA SAN DIEGO

The Effect of Crystallinity on the Corrosion Behavior of SAM2x5 Amorphous Steel *in situ* Composite

A Thesis submitted in partial satisfaction of the requirements for the degree Master of Science

in

Materials Science and Engineering

by

Nada Faisal Qari

Committee in charge:

Professor Olivia Graeve, Chair
Professor Javier Garay
Professor Marc Meyers

2019

The thesis of Nada Qari is approved, and it is acceptable in quality and form for publication on microfilm and electronically.

_____

_____

_____

Chair

University of California San Diego

2019

DEDICATION

I humbly dedicate this work to my parents, Faisal A Qari and Maha O Baryan. I wish there was a more heartfelt way to say thank for everything that you have done for me as no words of gratitude can ever be enough and I promise to work hard every single day of my life to make you proud.

And to H.E. Ali Al-Naimi, thank you for always inspiring me and for being the reason why I keep getting up no matter how hard I fall.

TABLE OF CONTENTS

LIST OF FIGURES

LIST OF TABLES

ACKNOWLEDGEMENTS

I would like to start by thanking Dr. Olivia Graeve for always offering her time and support throughout the project. Her valuable advice, experience and knowledge have always guided me towards the right direction while working as a graduate student in her lab. I have grown both personally and professionally while working with her and no words of gratitude could ever be enough.

Special thanks to Professor Garay and Professor Meyers for being part of my committee despite their extremely busy schedules. I truly appreciate their time, support and valuable advice which has added great value to my research and its progress.

Additionally, I would like to thank Arash Yazdani and Darren Dewitt for their help with sample preparation, microstructural analysis and intellectual discussions. The ability to complete my work within 10 months was purely because of their willingness to offer their valuable time and advice whenever I needed it. Without their support, this project could have easily taken more than 2 years to complete.

Thank you to Dr. Ekaterina Novitskaya for welcoming me into the Xtreme Materials lab with a big smile and wide arms. Her advice on safe lab practices, instrumental setup and sharing her valuable scientific opinion with me has added great value to my work and increased my safety awareness level in unmeasurable ways.

Furthermore, I would like to thank the MATS graduate advising team and members of the graduate division for guiding me throughout this incredible journey, without their help and support, I would have never made it this far.

I am eternally grateful to the University of Houston, where I completed my ungraduate studies, for playing a pivotal role in making me the professional that I am today. Special thanks to Dr. Vassiliy Lubchenko for mentoring me as an undergraduate researcher in his lab and for opening my eyes to the true value of scientific research. My time at the University of Houston has taught me that there are no limits to what we can accomplish through science as long as we have the perseverance to push the boundaries of human knowledge.

I would like to express my deepest gratitude to Saudi Aramco and my management back home in Saudi Arabia. Thank you for believing in me, empowering me and supporting me both financially and mentally. Thank you for always seeing something in me that I could never see in myself and for raising me up to more than I can be.

Finally, and most importantly, I would like to thank my parents, siblings, extended family members and dear friends for their never-ending encouragements and support despite being 8,272 miles away. Everything that I have achieved so far and all my future achievements are only possible because of you.

ABSTRACT OF THESIS

The Effect of crystallinity on the corrosion behavior of SAM2X5 amorphous steel in situ composite

by

Nada Faisal Qari

Master of Science in Materials Science and Engineering

University of California San Diego, 2019

Professor Olivia Graeve, Chair

The SAM 2X5 is a Fe-based bulk metallic glass with a chemical composition of $Fe_{49.7}Cr_{17.7}Mn_{1.9}Mo_{7.4}W_{1.6}B_{15.2}C_{3.8}Si_{2.4}$ which has a significantly higher resistance to corrosion when compared to its crystalline counterparts. In this research, dense samples were prepared using the spark plasma sintering technique at varying temperatures ranging from 630 to 675^{o}C which resulted in changing the the percent crystallinity of the samples from 20 wt.% to 82 wt.%, respectively. Corrosion rates of the specimens were measured in a 3.5% NaCl solution and it was found that by increasing

the sintering temperature and consequently crystallinity percent, the corrosion rate increases from 6.91 mpy (mils per year) to 13.01 mpy. Results of scanning electron microscopy showed that there were no significant microstructural changes in the amorphous matrix after the corrosion tests were completed, while the crystalline regions were severely corroded. It was found that the corrosion rate increased with increasing percent crystallinity. Yet, was still considerably lower than the control stainless steel sample which yielded a corrosion rate of 28.93 mpy under the same conditions.

Section 1. Introduction
1.1 The Global Challenge of Corrosion

Metallic structures including bridges, railways and pipelines are the building blocks of today's modern world because billions of users rely on them for transportation and meeting daily energy demands. Metals have been a common choice of materials in building and construction due to their durability and strength when used in forming structural components [1]. The most common metals include, Aluminum, Iron and Stainless-Steel [1].

Aluminum is the most abundant metal on planet earth and composes 8.1% of the earth's crust [2]. It is a silvery-white metal that is lightweight, soft, malleable and is rarely found in its pure form [2]. Usually, it's extracted from minerals using the Hall-Héroult process where aluminum oxide is dissolved in molten Cryolite, a halide mineral composed of Na_3AlF_6, and is electrolytically reduced to pure aluminum [2]. Aluminum is used in a variety of products ranging from airplane parts to kitchen utensils due to its low density, high thermal conductivity and ductility [2]. However, aluminum in its pure form is not that strong and it often used as an alloy [2]. When aluminum is alloyed with copper, magnesium or silicon, it becomes a lightweight strong material that is very important in the construction of airplanes and other forms of transportation [2].

Similarly, iron is the second most common metal on the planet and composes 5% of the earth's crust [3]. Iron in its pure form is a silver metal that is soft, easy to shape and is a good conductor of both heat and electricity [3]. However, it is very reactive towards oxygen and is naturally found in the form of oxides [3].

Therefore, there are seven type of iron oxides that differ based on the amount of iron present and they include, Hematite, Limonite, Goethite, Magnetite, Pyrite, Siderite and Taconite [3]. With a combination of underground and surface mining, the world produces a billion tons of iron oxides each year with 50% of the production taking place in China [3]. Because pure iron is too reactive, the iron used in construction and everyday items is in the form of an iron alloy [3]. These alloys are formed by mixing iron with other elements, especially carbon to form a stronger and more resilient material where the percentage of carbon determines the type of iron alloy formed along with its applications [3].

Steel is just a special type of iron alloy with a much lower carbon content than other iron alloys [3]. There are thousands of different types of steel that are designed for a particular application to perform a specific job under exact conditions [3]. The development of steel from iron involves three different stages starting with the conversion of iron to steel, followed by treating the steel to improve its qualities and finally, shaping the steel into the finished product [3].

In general, steel can be categorized into four different types: carbon steel, alloy steel, tool steel and stainless steel [3]. The vast majority of daily steel production is carbon steel, where steels with 1 to 2% of carbon are known as high-carbon steel while steels with less than 1% carbon are known as low carbon steel [3]. Alloy steel contains one or more elements such as chromium, copper, manganese, nickel, silicon or vanadium to provide an additional feature or an improved property when compared to carbon steel [3]. Tool steels are made of iron, carbon and added elements including nickel, molybdenum or tungsten to give them extra hardness so that they can be used

to develop tools, dies and machines parts [3]. Stainless steel is the most often used type of steel [3]. It contains a high portion of chromium and nickel which reduces the chemical reactivity of iron and increases the durability of the material making it a highly reliable material for building and construction [3]. In addition, it is very easy to clean, polish and sterilize which is why it is commonly used in household cutlery and medical instruments [3].

According to a study completed by the World Steel Organization this year, the world has consumed a total of 1.7 billion tons of steel in a wide range of applications [4] and as the world population continues to grow, cities will expand along with the demand for these metallic materials. Despite their durability and strength, these metals are highly reactive to oxygen which is one of their greatest shortcomings. Because this reactivity results in the inevitable deterioration that is caused by an electrochemical phenomenon known as corrosion. This makes maintaining the integrity of metallic structures a very difficult task but also a very vital task to ensure the safety of the billions of users who rely on them every day. However, this comes with a very high price tag and has shaped an industrial economic burden for many decades. In fact, the National Association of Corrosion Engineers (NACE) reports that the global cost of corrosion is estimated to be $2.5 trillion which is equivalent to 3.4% of the global GDP [5].

With a growing global population and increasing energy demands, the challenge and cost of corrosion will only continue to rise. Consequently, many research and development efforts have been focused on developing preventive solutions, control

practices and technologies that will assist in reducing these costs while meeting global demands.

1.2 Current Solutions and Corrosion Control Practices

With these figures in mind, the scientific community has developed multiple material-based solutions that are currently being used in multiple industries including building, construction and the energy sectors. The three most common solutions include protective coatings, cathodic protect and passivation.

Protective coating is based on the idea of applying a layer of paint or powder to act as a barrier and protect the metallic structure from corrosion [6]. The coating's ability to protect the metal and maintain its integrity heavily depends on the material selection, handling and application [6]. Paint based coatings are mechanically bonded to the surface of the metal through brushing or spraying and require the utilization of multiple layers with different formulations depending on the operating environment that the structure is exposed to [7]. In mild environments, single-coat systems are sufficient while severely corrosive environments require two to three layers of coating protection along with regular maintenance. An example of a common multi-layer coating system that is used to protect gas flare tips from its high exposure to hydrogen sulfide is based on an epoxy layer that Is sandwiched between a layer of zinc-rich paint and polyurethane [7]. Two factors govern the success of paint systems; adhesion and endurance. When the paint is not fully adhered to the surface of the metal, its ability to protect the metal and its endurance are compromised. Additionally, prior to application, the surface of the metal has to be prepared properly to ensure proper adhesion of the painted coating.

Similarly, powder coatings also provide the metal with a protective barrier. However, the process of applying them requires covering the surface of the metal with the powdered material followed by curing in an oven that converts the powder into a solid coating [8]. This can be achieved in two ways; spraying electrostatically charged powders on the metal surface or lowering the metal into a fluidized bed of the powder material. Powdered coatings are comprised of various materials that are designed to protect the metal from specific chemicals, abrasions and ultraviolet rays [8]. There are many technologies that are used to apply powdered coatings but the operating principle is mostly based on exposing the powder covered metal to high temperatures ranging from 375 to 400 ^{o}F to melt the powder [8]. After that, the coated metal piece is dried to ensure a durable coated finish. Just as is the case with paint coatings, the governing factor behind a successful powder-based coating is adhesion [8]. It is also critical to apply the powder in a consistent, uniform way that is free of any drips, bubbles or pores [8].

Cathodic protection is achieved by converting all of the anodic sites on the surface of the metal to cathodic sites to prevent corrosion [9]. This can be done by applying a layer of zinc which is more reactive than most metals when placed in a corrosive environment. When the coated structure is exposed, the zinc will react with oxygen from the corrosive environment and protect the structure from corrosion. This method is also known as a sacrificial system because the zinc layer is sacrificed to protect the structure from corrosion [9].

Passivation utilizes the formation of solid metal oxides during the corrosion process to protect the structure from further corrosion in a process commonly known as

self-passivation. In industrial practice, the formation of metal oxides on the surface of the metallic structure is accelerated by using a suitable oxidizing agent to treat the metal [10]. Common agents include, nitric acid and chromate solutions [10]. However, the reduction of the corrosion rate by passivation depends on the type of metal used and operating conditions [10].

By using preventative measures such as protective coatings, cathodic protection and passivation, an equivalent of $375 to $875 billion has been saved annually on a global basis which has resulted in reducing the global cost of corrosion by 35% [5].

Although these methods have been effective, they do have limitations including, ease of applicability, maintenance cost and degradation with time [5]. Hence, the search for alternative solutions continues along with new materials that will enable the future development of efficient and cost-effective corrosion prevention technologies.

1.3 Amorphous Metallic Alloys; A Potential Solution

1.3.1 An Overview of Amorphous Metallic Alloys

In recent years, investigations have shown that amorphous metallic alloys have unique properties. They are mechanically strong with high yield strengths and excellent magnetic properties [11]. Their thermal expansion coefficients can be close to zero in a wide range of temperatures making them excellent for electric resistance applications [11]. Additionally, iron-based amorphous alloys can resist corrosion at a much high rate than stainless steel with smaller amounts of chromium in the alloy mixture [11]. Other properties include superior elastic limits and high resilience when compared to their crystalline counterparts [12].

What distinguishes amorphous metallic alloys from other materials is their structure which gives them their unique properties. By definition, amorphous metallic alloys have a disordered atomic-scale structure [13]. As seen in figure 1, amorphous metals are non-crystalline and have a glass-like structure [13]. But unlike common glasses which are typically insulators, these amorphous metals have good electric conductivity [13].

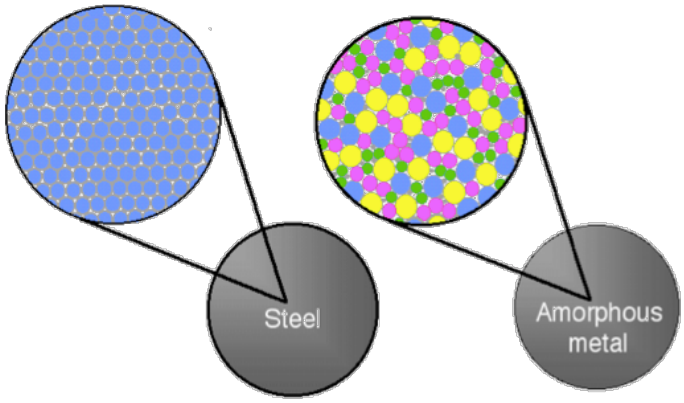

Figure 1. A magnification from the surface of steel and an amorphous metal which illustrates the structural difference between the two materials [14].

In general, amorphous metallic alloys can be divided into two groups based on composition: metal-metalloid alloys and metal-metal alloys [11]. The first group is composed of transition and precious metals including Iron (Fe), Cobalt (Co), Nickel (Ni), Rhenium (Re), Titanium (Ti) and Palladium (Pd) that are mixed with metalloids in an atomic content that ranges from 15% to 20% [11]. These metalloids include Boron (B), Carbon (C), Phosphorus (P), Silicon (Si) and Germanium (Ge) [11]. The second group is composed of binary alloys that are designed using transition metals, simple metals and rare-earth metals in varying ratios [11]. The second group of alloys can also be used to develop multicomponent amorphous alloys [11].

When it comes to processing and producing amorphous metallic alloys, different methods are used and can be divided into three processing techniques [11]. The first method utilizes vacuum evaporation, condensation, cathodic sputtering and gas-thermal sputtering [11]. The second method involves quenching from the liquid state, chemical deposition from the molten state and laser-induced vitrification [11]. The third and final method transfers crystalline solids into an amorphous state via ion implantation, neutron irradiation, mechanical action, pressure and solid-phased reactions [11].

The most common method to produce amorphous metallic alloys is the rapid quenching from the molten liquid state of the material. Quenching is defined as the rapid cooling of a liquid at a rate that range from 10^6 to 10^9 Kelvin per second [15]. Due to the extremely fast cooling rates, the structure of the liquid melt freezes in its non-crystalline states and results in the formation of an amorphous solid [15].

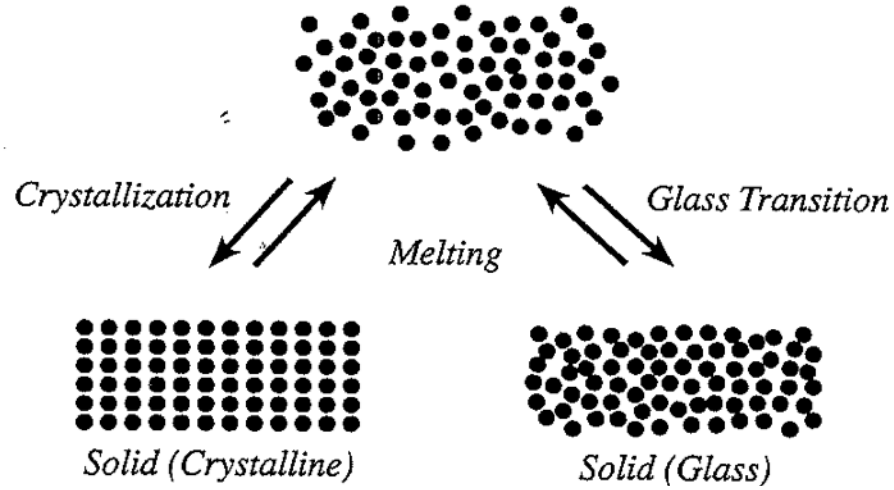

Figure 2. The difference between crystalline and amorphous solids based on cooling rate [16].

When solid materials are formed from the molten liquids, the cooling rate determines the morphology of the solid state as illustrated in figure 2. If the molten liquid state of the

material is cooled at a slow rate and is given sufficient time, it will solidify into a crystalline state. However, if the molten liquid is cooled at a rapid rate within a very short period of time, it will solidify into the amorphous glass state. Therefore, quenching is an effective way to produce solid amorphous metallic alloys because it provides the cooling rate required to freeze the liquid molten metallic alloy in its amorphous non-crystalline state.

Due to the availability of advanced processing technologies, amorphous metallic alloys have been produced on a large scale and are currently being used in commercial applications such as the development of high efficiency transforms and electronic article surveillance for theft control [17]. Nevertheless, applications have been limited due to the brittleness of amorphous metals at room temperature along with the limited understating of their structural complexity [12]. But with mass production, more research efforts have been focused on enhancing the properties of amorphous metallic alloys and developing structural models with the aspiration of unlocking many of their potential applications [12]. For example, recent efforts have produced Palladium and Zirconium based alloys with a strength of 1.6 GPa and a fracture toughness of 230 MPa.√m [12]. This record-breaking combination of strength and toughness has created the opportunity of using amorphous alloys in structural applications [12].

Another attractive property which makes amorphous metallic alloys suitable for structural applications is their high resistance to corrosion [17]. They can be used as metallic coatings to protect industrial structures from corrosion. However, the effect of heat treatment and thermal relaxation can drastically change the mechanical properties of amorphous metallic alloys. Yet, these effects are not well understood due to the

structural complexity of the alloys and multiple structural models have been developed to better understand how the structure and the unique properties of amorphous metallic alloys are related [17].

1.3.2 Structural Models of Amorphous Metallic Alloys

Amorphous metallic alloys can assemble in a variety of structures and multiple models were designed to study them. These topological models construct an amorphous structure from the solid crystalline and gaseous states based on the form of a polyhedral with atoms located at the vertices [11]. The existing models can be divided into three main groups based on the structural state of the starting material [11]. The first group of these models are the microcrystalline models which have short-range order characteristics based on the corresponding crystal lattices [11].

The second group is the cluster model which is similar to the microcrystalline model but the basic structural unit is a non-crystallographic ordered micro-cluster of atoms that play the same role as microcrystals. Based on this model, there are two possible arrangements: a thirteen-atom icosahedron and pentagonal dodecahedron. An illustration of both structures is provided in figure 3 [11].

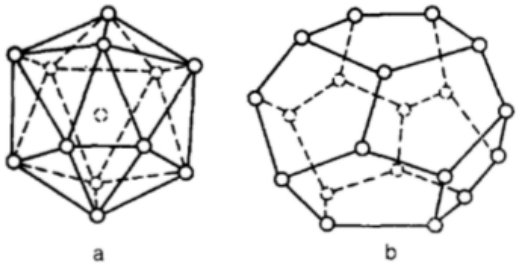

Figure 3. The two possible microcrystal arrangements where (a) is the thirteen-atom icosahedron and (b) is the pentagonal dodecahedron [11].

The third group is based on the development of a continuous random network through a combination of random closed packing rigid and soft spheres [11]. It is based on a modified version of the random packing of atoms that is applied to covalent and oxide glasses [11]. All models of this group are characterized by a collection of equal sized spheres or two different sizes that are packed randomly and relaxed to the highest density [11]. The models within this group differ by packing rules, interaction potential and the method of relaxation [11]. The structural elements of crystallographic and non-crystallographic packing can be distinguished when looking at multiple configurations of random closed pack models by using the Bernal polyhedral depicted in figure 4 [11].

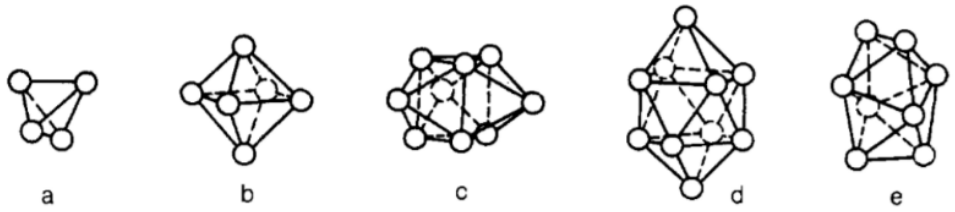

Figure 4. Configuration of atoms in the close packing based on the Bernal polyhedral where (a) is a tetrahedron, (b) an octahedron, (c) a trigonal prism, (d) Archimedean antiprism and (e) a tetragonal dodecahedron [11].

Analysis of these three different model groups have shown that there are many similarities between the microcrystalline and cluster model because both models build their structures using structural units with different topologies [11]. Additionally, other models have been developed to construct amorphous metallic alloys that are rapidly cooled from the liquid state. These models create structures based on the configurational characteristics of the liquid state [11]. The analysis of these structures is conducted using a Voronoĭ polyhedral where that atoms occupy the sites inside the

polyhedron instead of the vertices [11]. This model has recently been used to study a metal-metalloid alloy and results have shown that coordination around the metal atoms where represented by distorted icosahedra while the coordination around the metalloid atoms was represented by a more energetically favored structure including distorted octahedron and trigonal prisms [11].

By using general indices, it is possible to classify a structure with a short-range ordered atom arrangement including the structure of amorphous metallic alloys with the help of topological and Voronoĭ polyhedral models [11].

1.3.3 Structural Relaxation of Amorphous Metallic Alloys

With the development of the models discussed in the previous section, a better understanding of the structure of amorphous metallic alloys was attained allowing for further investigation on how it effect the properties of the alloys. Furthermore, recent research efforts have found that despite the process used to prepare an amorphous metallic alloy, its structure is not in a metastable state of equilibrium and the transition into the metastable state is accompanied by a change in the physical properties [11]. An example of such a transition is observed when an amorphous alloy is heated or isothermally annealed at a temperature that is below its glass transition temperature that results in increasing the density and elastic modulus while decreasing the diffusional coefficient [11]. The observed change in properties is connected to a process known as structural relaxation, where the amorphous structure relaxes to a state of metastable equilibrium. During structural relaxation, atomic displacement takes place and results in changing the interatomic distance between the nearest neighbors along with the average interatomic distance and chemical order [11].

X-ray diffraction data were collected for an amorphous alloy with a chemical composition of $Fe_{40}Ni_{40}P_{14}B_6$ to confirm the physical changes that accompany structural relaxation. By analyzing the XRD spectrum, it was observed that the peaks in the structural factor curves become higher and narrower indicating a significant change in the structure of the alloy [11]. Additionally, structural relaxation is caused by the motion of atoms which results in re-ordering the nearest-neighbors around a particular atom and changing the density along with the physical properties of the alloy [11]. These results are not unique to the $Fe_{40}Ni_{40}P_{14}B_6$ alloy and have been observed in other amorphous metallic alloys [11].

A better understanding of structural relaxation can be achieved by looking at the free energy diagram of an amorphous metallic alloy that was produced by quenching from the liquid state. Figure 5 represents the dependence of free energy (F) on temperature (T) and volume (V) which act as structural parameters when the material is in a condensed state [11].

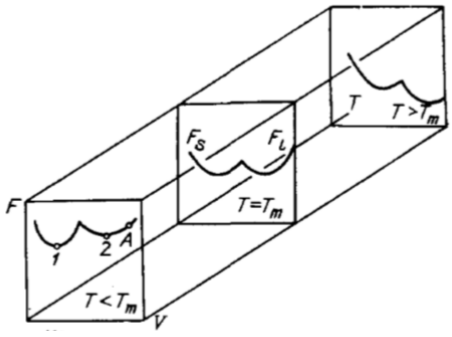

Figure 5. The free energy of a condensed state as a function of temperature and volume [11].

The dependence of free energy on the volume is illustrated as a potential well for the solid crystalline state (F_s) and the liquid state (F_L). Additionally, the dependence of the

free energy on volume indicates that the energy of the system is minimized at the state of equilibrium [11]. At temperatures above the melting temperature (T_m), the bottom of the potential well F is lower for the liquid state. However, when the temperature is below T_m, the potential well F is lower for the solid crystalline state [11]. When the system is rapidly quenched, a super cooled liquid state is achieved and can be described by point 2 at $T < T_m$ in figure 5 [11]. When the temperature is below the glass transition temperature (T_g), the structure freezes and the system is characterized by point A at $T < T_m$ in figure 5 [11]. At point A, the system is in a non-equilibrium state and would prefer being in the metastable state depicted by point 2. The transition process from point A to point 2 is the process of structural relaxation that is observed in amorphous metallic alloys. It is important to energetically distinguish between the relaxation and the crystallization processes. Relaxation takes the material to a metastable state while crystallization transitions the material into a state of absolute minimum energy that is illustrated by point 1 at $T < T_m$ in figure 5 [11].

As stated previously, volume is a structural parameter that is affected by temperature and the transition associated with the equilibrium and metastable states. It is also connected to the vibration of atoms and the change of defect concentration which determines the type of vacancies that can occur in amorphous metallic alloys [11]. Furthermore, recent findings have revealed that structural defects have a direct effect on the properties of amorphous metallic alloys and the details of these effects are discussed in the next section.

1.3.4 Structural Defects in Amorphous Metallic Alloys

By understating the process of structural relaxation and the development of advanced structural models, more research efforts have been focused on the studying the properties of amorphous metallic alloys. Recent findings confirm that these alloys are structurally sensitive to the preparation conditions, particularly, the conditions of heat treatment and other external actions [11]. These effects have been investigated through structural relaxation of amorphous metallic alloys where the alloys experience changes in there mechanical, electrical and magnetic properties [11].

Similar to crystalline structures, the structurally sensitive properties of amorphous metallic alloys are determined by the defects that are present in the amorphous structure [11]. However, crystalline structures have a long-range ordered arrangement of atoms while amorphous structures have short-range ordered arrangement of atoms [11]. Based on that, an ideal amorphous structure is defined as a structure that does not have any form of disruption in its short-range ordered arrangement [11]. When such disruptions are present in the amorphous structure, they act as structural defects and have a direct impact on the properties of the alloy [11]. When the size of these defects is less than 1 nm, they are considered point defects and they include: free volume fluctuations, n-type, p-type and vacancies. P-type defects appear in parts of the alloy with high local density while n-type defects appear in low density areas [11]. N-type defects also create local fluctuations that generate excess free volume which acts as another type of defect [11].

Coordination number is another important factor when studying the structural sensitivity of amorphous metallic alloys. It can act as a defect when a local section of

the amorphous alloy has a different coordination number than the idea Z-coordination of the alloy [11]. Based on this definition, the simplest coordination number of a defect is when one of the atoms has a coordination number that differs by one unit from the ideal Z-coordination [11]. Defects of this type can occur as a collection of simple defects with coordination (Z – 1) or (Z + 1) for the surrounding atoms [11]. These types of defects can exist only in amorphous structures and different combination can result in the formation complex point defects [11].

Defects at the microscopic level can also occur in amorphous metallic alloys including line defects and disclinations, which are a special kind of line defects where rotational symmetry is violated [11]. There sizes range from 10 to 100 nm and can only occur in a space of constant curvature such as a three-dimensional sphere. Therefore, in order to create microscopic defects in an ideal amorphous metallic alloy, line defects must be introduced into the structure of the alloy with nuclei that consist of clusters that differ from the icosahedral symmetry [11]. Diffraction investigations have been used to prove the effect of defects on the properties of amorphous metallic alloys and recent findings have confirmed that defects with a distinguished type of short-range order begin to experience phase separation which negatively effects the unique properties of the alloys [11].

In addition to nano and micro defects, the partial crystallization of amorphous alloys can also cause phase separation and negatively impact some of the highly desired properties of the alloys such as their high ability to resist corrosion. However, these effects are not well understood and further investigations are necessary to determine the main reasons behind these effects. Therefore, the objective of the current

is study is to determine the effect of temperature and crystallinity on the corrosion behavior of an iron-based amorphous metallic alloy known as the SAM 2X5 composite.

But before discussing the experimental setup and the results of the current study, a brief background on the development of amorphous metallic coatings, corrosion, crystallization and how they are related when studying amorphous metallic alloys is provided in the following sections along with an introduction on spark plasma sintering, a densification technique that was used to prepare solid samples of the iron-based amorphous metallic alloy investigated in this study.

1.3.5 Application; Designing Amorphous Metallic Coating

Amorphous metallic alloys have the potential of being used in the development of a high-performance coating due to their unique properties and high resistance to corrosion. To achieve this, powdered metals need to be converted into solid coatings which can be accomplished through thermal spraying technologies. These technologies are used in industry to develop metallic and ceramic coatings with high hardness, strong adhesion with substantial wear resistance and corrosion protection [18]. The process of converting a powdered material involves using multiple tools and equipment with the most common process being the “High-Velocity Oxygen Fuel Thermal Spray” that is also known as HVOF. The main reason HVOF is commonly used in thermal spraying applications is due to its ability to form a strongly adhered coating (up to 95 MPa) in an efficient and cost-effective manner [19].

The HVOF spraying technology is based on a deposition process of micro-sized metallic/ceramic particles [19]. These particles are heated in a supersonic combusting gas stream to produce a molted deposition that is applied on the surface of the

substrate using a high-speed stream to form a layer of coating as illustrated in figure 6 [20].

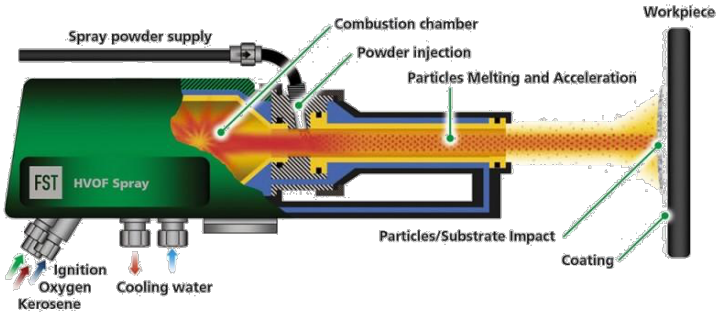

Figure 6. The main components of the thermal spraying tool that is used when coating a substrate via the HVOF process [21].

The thermal spraying process using HVOF begins with the ignition of a kerosene/oxygen mixture in the composition chamber where a powdered material is supplied through a nozzle [22,20]. The ignited kerosene/oxygen mixture is released creating a jet stream with very high temperatures [22,20]. This rapid increase in temperature causes combustion that melts the powdered particles. After that, compressed air is used to deposit the molten particles on the surface of the substrate with very strong adhesion [22].

Section 2. Background

2.1 The Fundamentals of Corrosion
2.1.1 The Chemistry of Corrosion

By definition, corrosion is the thermodynamically spontaneous degradation of a reactive material by an aggressive environment [23,24]. In the case of metals, it occurs by the simultaneous oxidation of the metal (at the anode) and reduction of dissolved oxygen (at the cathode) as illustrated in figure 7 [23,25].

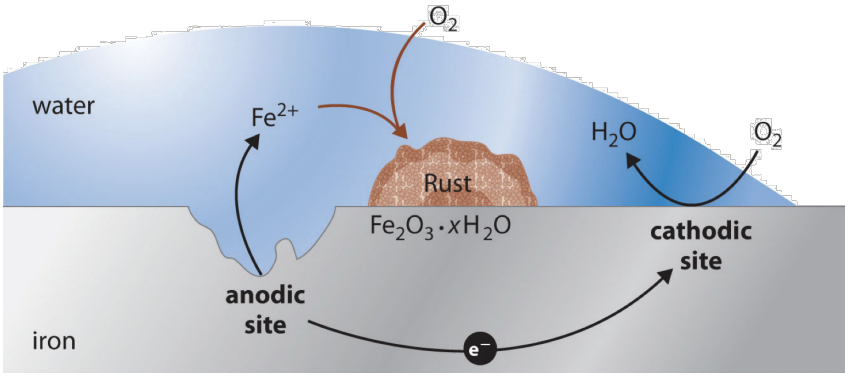

Figure 7. Diagram that illustrates the corrosion process along with the half reactions that take place on the surface of the metal [26].

The redox reactions that take place on the surface of the metal when exposed to a corrosive environment are described by equations 1 through 3 [9]:

$$2\ Fe \rightarrow 2Fe^{2+} + 4e^{-} \quad \textbf{(1)}$$

$$O_2 + 4e^{-} + 2H_2O \rightarrow 4\ OH^{-} \quad \textbf{(2)}$$

$$2Fe + O_2 + 2H_2O \rightarrow 2Fe(OH)_2 \quad \textbf{(3)}$$

Based on equation 1, free electrons travel from the anode through the metal towards the cathode where oxygen gas is converted into an oxygen ion. The formation of the oxygen ion is accomplished by the reduction reaction described in equation 2 where the

oxygen gas reacts with four electrons and water to form the hydroxyl ion. The recombination of the hydroxyl and iron ions on the active metallic surface is described by equation 3. The product of this reaction is known as ferrous hydroxide, where iron combined with oxygen and water result in the formation of ferrous hydroxide $Fe(OH)_2$ [9]. Since, these partial reactions are charge-transfer processes, the corrosion phenomenon is essentially electrochemical in nature [25] and can be experimentally studied using electrochemical techniques.

2.1.2 The Five Types of Corrosion

Corrosion can be classified into five categories based on the appearance of the damaged corroded metal and each form can be identified by visual observation. Only by carful observation of the corroded surface can the required information be collected to develop the appropriate solution for the specific type of corrosion that the metal is experiencing [27].

The first type is uniform general attack corrosion which is the most common form of corrosion. It is characterized by the electrochemical reactions described in the previous subsection that takes place uniformly on the exposed surface of the metal. As the reaction progresses, the metal becomes thinner and eventually fails. General corrosion is the greatest destruction of metal on a tonnage basis [27]. However, the service life of metallic structures can be accurately estimated by using simple tests. Therefore, it is not a big concern in industrial practice and can easily be prevented using protective coatings and cathodic protection [27].

Galvanic corrosion occurs when there is a potential difference between two dissimilar metals that are exposed to a corrosive or a conductive solution [27,28]. The

potential difference between the two metals generates an electron flow [27,28]. This results in increasing the corrosion rate of the less stable metal while decreasing the corrosion rate of the more stable metal. The two metals form a galvanic couple, where the less stable metal acts as the anode and the more stable metal acts as cathode [27,28]. When the corrosion reaction takes place, the cathodic metal experiences very little corrosion while the anodic metal experiences sever corrosion.

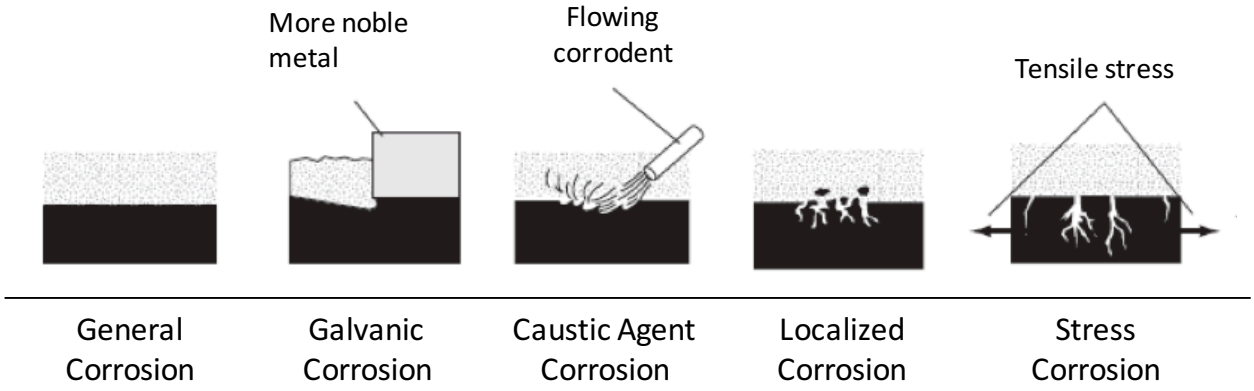

Figure 8. The five different types of corrosion (illustrated in light gray) that can take place on the surface of the metal (illustrated in black) based on the different metals and operating environments [29].

The exposure of impure gases to a moist environment results in the formation of harmful corrosive droplets which act as caustic agents with hydrogen sulfide as an example [27]. Although, dry impure gases don't cause damage to metallic materials, they can wear them down when they are converted to caustic agents through caustic agent corrosion [27].

When small parts of the metal undergo corrosion at a faster rate than other parts, the metal is experiencing localized corrosion. This commonly occurs at grain and phase boundaries because they are slightly more reactive than the metal matrix [27]. It is most commonly caused by impurities at the grain boundaries or the depletion of a corrosion

inhibiting element [27,30]. Since small parts of the metal exhibit corrosion at a faster rate, its effect works with other damaging processes such as stress and fatigue leading to the catastrophic failure of the metallic material that is experiencing localized corrosion [27].

Materials that are subjected to extreme tensile stress experience a destructive type of corrosion known as stress-corrosion cracking [27]. This type of corrosion attacks the material along the cracks that are formed due to the stress applied. Stress cracking corrosion is intensified at high temperatures and sever operating conditions which results in causing irreparable damage to the metallic structure [27].

2.1.3 Studying Corrosion Using a Corrosion Test Cell

The understanding of how different materials behave when exposed to a corrosive environment is essential when designing industrial structures and developing corrosion prevention solutions. Experimentally, this is accomplished by placing a small sample of the desired material in a three-electrode corrosion test cell to study the corrosion behavior of the material [31]. As the name suggests, the cell is composed of three different electrodes; a reference, counter and working electrode, where each one has a specific function [31].

The reference electrode is an electrode that has a stable and well-known electrode potential [32]. In an electrochemical experiment, it is used as a half cell that allows for the potential of the material being tested to be measured. There are three different types of reference electrodes; a standard hydrogen electrode (SHE), a saturated calomel electrode (SCE) and a silver-silver chloride electrode (Ag/AgCl) [33].

The standard hydrogen electrode has a simple design that is based on an inert solid like platinum that has the ability to adsorb hydrogen gas when immersed in a

solution that contains hydrogen based on the half reaction described by equation 4 with a potential that is equal to zero Volts [33].

$$2H^{+}_{(aq)} + 2e^{-} \rightleftharpoons H_{2\ (g)} \qquad \textbf{(4)}$$

Despite its simple design, the application of the SHE is very limited due to the requirement of using hydrogen gas in the half cell reaction and to maintain the functionality of the electrode [33].

Although the saturated calomel electrode is used more often than SHE, it is toxic due to the utilization of mercury in its design. The half-cell is composed of mercurous chloride (Hg_2Cl_2) that is in contact with a pool of mercury [33]. The assembly of these components is based on a design called the double-junction arrangement, where the components are placed within a fritted compartment that is surrounded by potassium chloride (KCl) solution. Another way to assemble them is to layer them under a saturated KCl solution and a platinum wire is used to connect the SCE electrode to the external circuit. The half reaction of the SCE is described by equation 5 and the utilization of the SCE provides the cell with a reference potential that is equal to +0.244 Volts [33].

$$Hg_2Cl_{2(s)} + 2e^{-} \rightleftharpoons 2Hg_{(l)} + 2Cl^{-}_{(sat'd)} \qquad \textbf{(5)}$$

A common way to assemble the SCE electrode is illustrated in figure 9 where a paste of Hg_2Cl_2 is immersed in a saturated KCl solution.

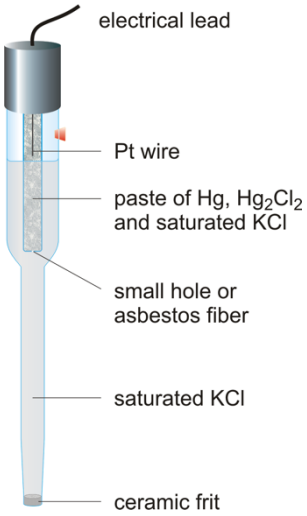

Figure 9. Common assembly of a saturated calomel electrode [34].

The silver/silver chloride electrode is designed by immersing a silver wire that is coated with a layer of solid silver chloride in a solution of KCl and AgCl. The half-cell reaction is described by equation 6 which provides the cell with a potential that is equal to +0.222 Volts [33] and the final assembly of an Ag/AgCl electrode is illustrated in figure 10.

$$AgCl_{(s)} + e^- \rightleftharpoons Ag_{(s)} + Cl^-_{(sat'd)} \qquad \textbf{(6)}$$

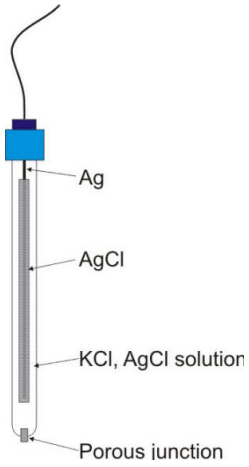

Figure 10. Common assembly of a silver/silver chloride electrode [35].

Both the saturated calomel electrode and silver/silver chloride electrode provide the corrosion test cell with stable half-cell potentials that do not change over time or with varying temperature conditions. The ability to utilize reference electrodes in a corrosion cell make it possible to measure the potential and the corrosion behavior of any conductive material.

In a corrosion testing cell, the working electrode is composed of a small sample of the material being tested. The sample can be bare metal, coated metal or a metallic alloy. Once the sample is placed in the cell, an electrochemical reaction occurs on the surface of the working electrode by applying a fixed potential between the reference and working electrodes [36]. This reaction generates a current that is balanced by another current that is flowing in the opposite direction at the counter electrode [32,36]. Because of its function of balancing and closing the current circuit, the counter electrode is made

of inert materials such as platinum, graphite or glassy carbon so that it does not participate in the electrochemical reaction [32]. Together, the three electrodes are assembled as illustrated in figure 11 to form a corrosion test cell.

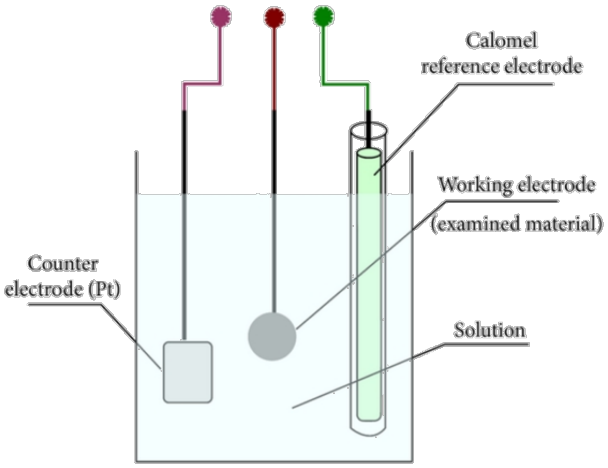

Figure 11. A corrosion test cell that is designed using a counter Pt electrode, a SCE reference electrode to study the corrosion behavior of a metallic disc that is used as a working electrode [37].

The utilization of an electrolyte is required to drive the electrochemical reaction on the surface of the working electrode [38]. The electrolyte has two main functions; first, it provides the required conductivity between the cathode and anode [38]. Second, it transports reactants to the electrodes and the products away from them [38]. Therefore, it is necessary to immerse the three electrodes in an electrolyte solution when conducting a corrosion test. A solution that is commonly used is a 3.5vol.% Sodium Chloride (NaCl) solution because it is an effective electrolyte and provides high salinity which stimulates a corrosive environment [31].

2.1.4 Electrochemical Analysis

When the corrosion cell setup is complete, the electrodes are connected to an electronic instrument called the potentiostat. This device is essential when it comes to analyzing data that are collected during an electrochemical experiment because it measures and controls the voltage difference between the working and reference electrode [39]. It also measures the current flow between the working and counter electrodes [39]. Once the potentiostat collects the data during the experiment, it transfers it to a supporting software titled “Echem”.

The Echem software is equipped with multiple ready-to-use functions that give the user the ability to calculate impedance, resistance and the corrosion rate of materials with the corrosion rate analysis being the most effective way to study the behavior of materials. The rate analysis experiment is effective because it provides the user with a comprehensive idea of how fast the material will deteriorate when operating in a corrosive environment which is critical when it comes to determining the lifetime of industrial structures.

The Echem software calculates the corrosion rate based on equations 7and 8 highlighted below [23,40]. First, the current data collected by the potentiostat are used to determine the corrosion current (I_{Corr}) as described by equation 7. Then, the calculated values of the current along with dimensional parameters of the tested sample are plugged into equation 8 to determine the corrosion rate (C_R) of the sample [40]. All the parameters used in equations 7 and 8 are defined in table 1.

$$I_{Corr} = \left[\frac{\beta_a \beta_c}{2.303\,(\beta_a + \beta_c)} \right] \left(\frac{1}{R_P} \right) \quad \textbf{(7)}$$

$$C_R = I_{corr}\, K\, W_s / d\, A \quad \textbf{(8)}$$

Table 1. The parameters used in equations 1 and 2 [40].

Parameter	Definition
I_{Corr}	The corrosion current in Amperes
β_a and β_c	Constants related to the cathodic and anodic partial reactions
R_p	The polarization resistance measured in Ohms
C_R	The corrosion rate
K	A constant that defines the units of the corrosion rate
W_s	Weight of the sample in g,
D	Density of the sample in g/cm^3
A	The area of the sample in cm^2

The unit of the corrosion rate (C_R) is determined based on the selected value of K as indicated in table 2 with the most common unit being mils per year (mpy) [31,40].

Table 2. The various units of corrosion rate that can be used based on the values of K [40].

Units of C_R	Value of K used
mm/year	3272
μm/year	3.272×10^6
Mils/year	1.288×10^5

Once the Echem software completes all the required calculations, it generates a graph which plots the corrosion rate in selected units versus the time in seconds. Theoretically, the graph should start with a low value and increase as the current flows through the sample for longer periods of time as seen in figure 12 and the actual corrosion rate of the sample is based on the first data point collected from the graph [41].

However, the Echem software provides the user with a function that calculates the average corrosion rate of the sample. The average value is more reliable when studying metallic alloys because their structural complexity causes divergence from the theoretical trend observed in figure 12.

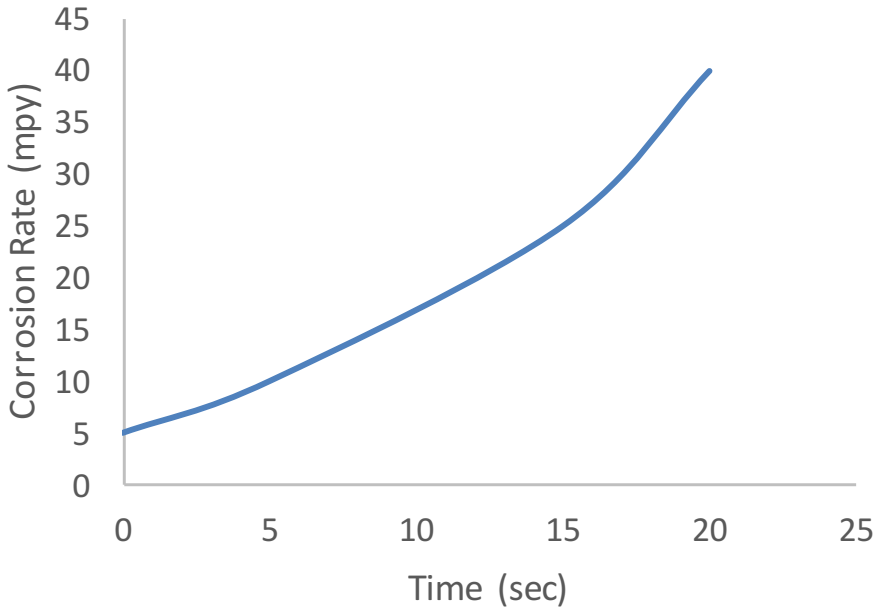

Figure 12. A theoretical graph of the corrosion rate in mils per year (mpy) vs. time in seconds for a general metal sample.

2.2 Crystallization of Amorphous Metallic Alloys

2.2.1 The Effect of Temperature on the Structure of Amorphous Metallic Alloys

In material science, crystallization is defined as the solidification of liquid atoms into a highly structured form called a crystal [42]. The process of crystallization involves two steps; the nucleation of atoms that is followed by crystal growth. During the nucleation step, atoms cluster together on a microscopic scale to form a stable crystal nucleus [42]. Nucleation of a parent phase can be heterogeneous or homogeneous. When the nucleation of a parent phase involves a reaction with a foreign substance, it's known as heterogeneous nucleation [43]. But when the interior of the parent phase experiences nucleation without the involvement of an exterior substance, it's considered homogeneous [43]. Crystal growth begins when the nucleation process has resulted in

the formation of a stable nucleus that can grow given sufficient time to produce the final crystal [42]. However, the crystallization process of amorphous solids is a complex process that involves the simultaneous nucleation and growth of crystallites [43].

The driving force for crystallization is the difference in Gibbs free energy between the amorphous and crystalline phase [43].

$$\Delta G = \Delta H - T\Delta S \qquad \textbf{(9)}$$

$$\Delta G = \frac{L}{T_m}(T-T_m) \qquad \textbf{(10)}$$

Equation 9 is a mathematical description of the difference in Gibbs free energy based on enthalpy (H), temperature (T) and entropy (S). In equation 10 the description is defined purely by temperature (T and T_m) and the latent heat of fusion (L) [43]. Both equations show that crystallization has a clear dependence on temperature.

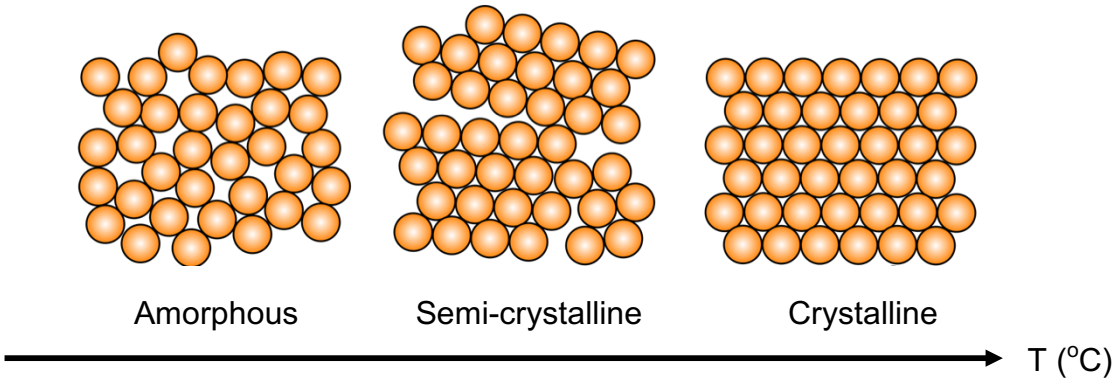

Figure 13. The effect of high temperature on the amorphous structure of materials [44].

An increase in temperature will result in a higher crystallization rate and a higher weight percent crystallinity within amorphous metals. Additionally, as temperature goes up, the activation energy of crystallization decreases [43]. This means that a group of atoms in the amorphous state require less energy to jump to the crystalline state [43].

Therefore, the sample becomes less stable in the amorphous state and is more likely to crystallize.

2.2.2 The Development of Corrosion Active Zones

As the percent crystallinity increases, the microstructure of an amorphous metallic alloy will begin to separate into crystalline and amorphous regions.

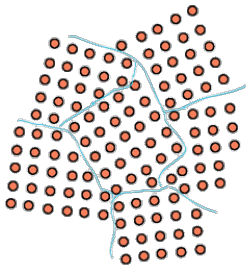

Figure 14. The formation of crystalline regions creates boundaries (blue lines) between the different phases of the parent material [45].

The boundaries between the two regions give rise to localized Intergranular corrosion [30,43] and will result in negatively effecting the amorphous metal's ability to resist corrosion. When an amorphous metal with a high percent crystallinity is exposed to a corrosive environment, Intergranular corrosion will attack along the boundaries or areas that are adjacent to them while the bulk of the sample remains unaffected as seen in figure 15 (a).

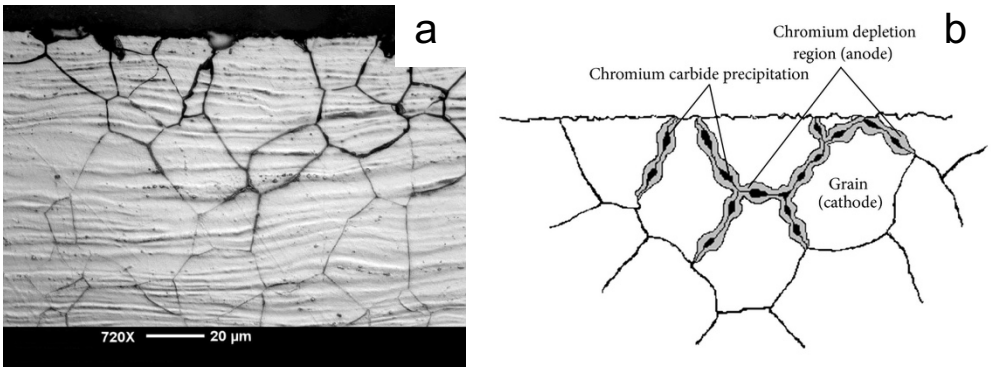

Figure 15. SEM image showing the localized effect of Intergranular corrosion along the boundaries (a) [46] and a schematic that shows an increased corrosion rate along the depletion zones (b) [47].

The attack occurs due to the segregation of specific elements or the formation of compounds along the boundary [30]. Intergranular corrosion occurs by preferential attack on the boundary phase or an area that is adjacent to it that has lost an element necessary for adequate corrosion resistance such as chromium which results in the formation of a depletion zone as seen in figure 15 (b) [43]. This zone acts as an anodic site relative to the reminder of the surface and the attack progresses along the boundary which will experience a higher corrosion rate than the reminder of the sample [30].

Although the impact of Intergranular corrosion begins on a microscopic level, it can accelerate rapidly and damage the material on a macroscopic level that is visible to the naked eye as seen in figure 16.

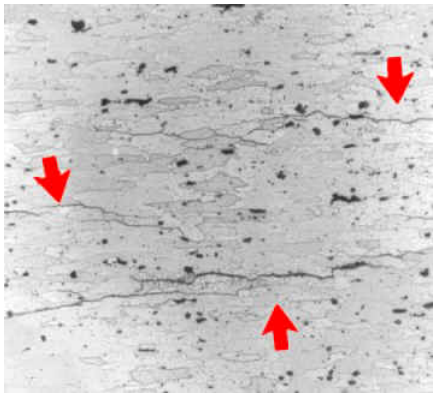

Figure 16. Intergranular corrosion of failed aircraft component made of 7075-T6 aluminum [30].

An aircraft component that was designed using a specific type of aluminum suffered from Intergranular corrosion that accelerated to a point beyond repair and resulted in the failure of the part seen in figure 16. Therefore, it is essential to control Intergranular corrosion when developing materials for structurally critical applications by minimizing phase boundaries and depletion zones [46].

2.3 Spark Plasma Sintering (SPS)

2.3.1 Definition of Spark Plasma Sintering

Sintering is a process that involves the consolidation of powders at $T > 0.5T_m$ where the diffusional mass transport leads to the formation of a dense body [48,49]. Thermodynamically, the driving force is the decrease of the total free energy of the system by decreasing the total surface area [48]. This is accomplished by replacing the solid-vapor interface with a solid-solid interface [48]. This can be mathematically defined by the Gibbs free energy as described in equation 11 [48].

$$dG = \gamma_{ss} dA_{ss} + \gamma_{sv} dA_{sv} < 0 \quad \textbf{(11)}$$

Sintering is an irreversible process which will stop when dG equals zero and equilibrium is achieved. The basic phenomenon that occurs during the sintering process is illustrated in figure 17 and is driven by the change in surface energy.

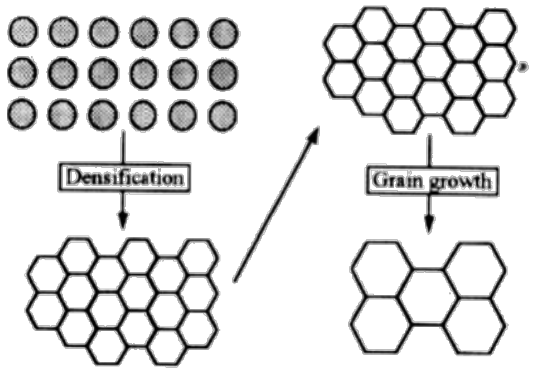

Figure 17. The basic phenomena which occur during sintering based on the driving force described in equation 11 [50].

2.3.2 Working Mechanism

The working mechanism of spark plasma sintering is based on compacting a powdered material by using a graphite die and passing an alternating current through the graphite die/powder assembly [48,49]. The presences of high pressure and an electric current gives rise to Joule heating which causes localized necking and the densification of the powder to occur within a few minutes as illustrated in figure 18.

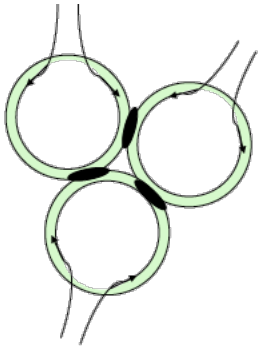

Figure 18. Powdered particles experiencing localized necking at a faster rate than conventional methods due to Joule heating [48].

By definition, Joule heating is the process of generating heat when an electric current passes through a conductive material. This makes the heating source in spark plasma sintering internal when compared to other conventional densification techniques such as hot pressing where the heating source is external [48]. An internal heating source provides a very high heating/cooling rate which is why the densification of powders using spark plasma sintering is very fast and achievable at low operating temperatures [48,51]. Because the SPS process is very fast, it has the ability to densify nanoscale powders while minimizing the coarsening of powdered particles which commonly occurs when employing standard densification processes. Additionally, this has made SPS an excellent technique that is used to densify a wide range of materials including nanoparticle ceramics and metallic alloys [48].

The densification mechanism can be explained by three different stages. In the first stage, the powdered particles experience surface tension due the high pressure and begin to neck [51]. The second stage is when the surface begins to experience overheating which causes the acceleration of the necking rate [51]. The third and final stage involve the diffusion of grain boundaries and lattices which leads to the formation of the solid dense body [51]. These transition stages are clearly seen by the SEM images in figure 19.

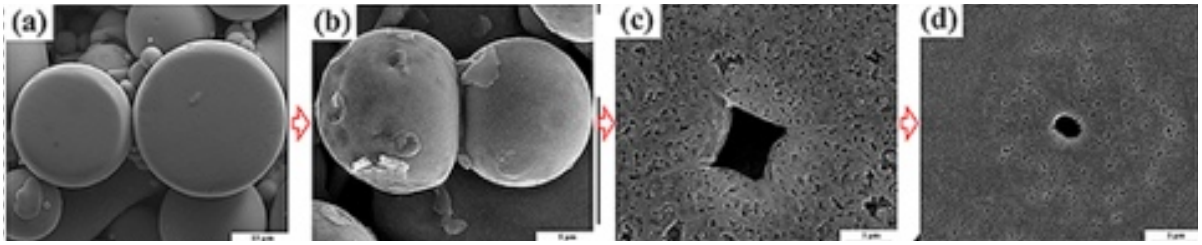

Figure 19. SEM images that show the multiple densification stages; where (a) and (b) illustrate stage 1, (c) illustrates stage 2 and the final stage is shown in (d) [51].

The rate limiting step in the densification mechanism is the diffusion of the slowest diffusing ion along its fastest path while surface diffusion can result in coarsening of the particles [48].

2.3.3 Instrumentation

When sintering powdered materials, they are compacted using a graphite die as illustrated in the center of figure 20. On both sides of the sintering chamber, a load of 30 kilo Newtons is applied on the sample to reach the pressure required to densify the powder [52]. Using a current generator, an electric current is applied which passes through the graphite plates to reach the graphite die and powder inside the sintering chamber [52].

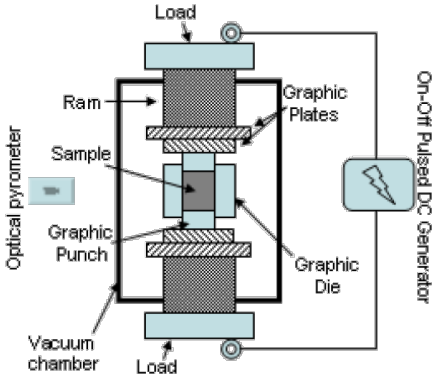

Figure 20. Diagram showing the main parts of the spark plasm sintering machine that is used to densify powdered materials [48].

The sintering experiment is completed under vacuum to protect the powder from any atmospheric chemical interactions that may occur and to prevent the formation of undesired products [52].

Section 3. Experimental Procedure

The SAM 2X5 addressed in the current study is a Fe-based amorphous metallic alloy with a chemical composition of $Fe_{49.7}Cr_{17.7}Mn_{1.9}Mo_{7.4}W_{1.6}B_{15.2}C_{3.8}Si_{2.4}$. Bulk samples were prepared via SPS in the shape of a disc with a diameter of 1.8 cm, a thickness of 1 mm and a mass of 2.5 g. Samples were sintered at different temperatures ranging from 630 to 675^{o}C with varying densities and percent crystallinity as specified in table 3. The percent crystallinity was calculated based on equation 12 [53] while the values of temperature and density were collected from data generated by the SPS instrument.

$$\%C = \frac{v_{amorphous} - v_{partially\ crystalline}}{v_{amorphous} - v_{totally\ crystalline}} \qquad \textbf{(12)}$$

Where v is the specific volume in cm^3/g of the SAM 2X5 composite in the amorphous, partial and total crystalline states.

Table 3. The sample number, sintering temperature, percent crystallinity and density of the experimental samples.

Sample number	Temperature (^{o}C)	% Crystallinity	Density (g/cm^3)
NQ # 1	630	20	7.50
NQ # 2	645	42	7.62
NQ # 3	660	61	7.84
NQ # 4	675	82	7.75

Each sample had a surface area of 2.54 cm^2 and in preparation for the corrosion rate analysis, each sample was polished using the TED PELLA XP 8 polisher and premium SiC abrasive discs for four cycles with varying roughness. The first cycle started with a roughness of 240 grit followed by 600 grit and 800 grit cycles. The polish was finalized with a roughness of 1200 grit. Each cycle lasted for 10 minutes and the sample was rotated by 90^o at the beginning of each cycle to ensure the smoothness of the tested surface.

The corrosion rate analysis was conducted using a three-electrode corrosion test cell and by immersing the samples in a 3.5 vol.% NaCl salt solution. The solution was prepared by mixing 7.56 g of sodium chloride NaCl (purchased from Fisher Chemical S271-500) with 100 mL deionized water using a magnetic steering rod for 10 minutes in a 150 mL beaker. Before immersing the sample in the salt solution, a 15 cm copper wire was wrapped around the dimeter and was used to connect the sample to the corrosion test cell.

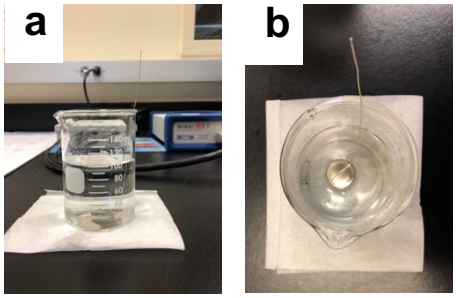

Figure 21. a) How the SAM disc is immersed into the salt solution with the copper wire warped around it b) a top view image of the setup.

The test cell was composed of a Gamry Interface 1010 E potentiostat, an Ag/AgCl reference electrode, a graphite counter electrode and two working electrodes. The cell's circuit was completed by connecting the copper wire to the two working

electrodes and the final setup of the corrosion test cell is illustrated in figure 22. It is important to note that when the sample was immersed in the salt solution along with the counter and reference electrode, they did not come in to contact with each other during the test because this would have resulted in overloading the cell and generating unnecessary noise in the spectrum.

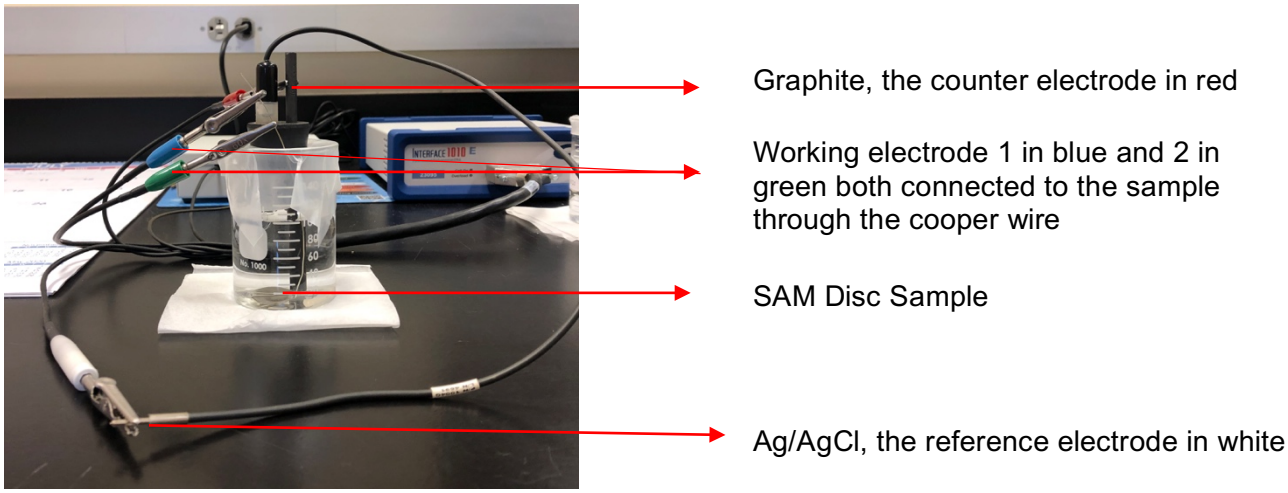

Figure 22. The final setup of the corrosion cell with the immersed sample connected to the potentiostat.

Section 4. Corrosion Rate Analysis

The objective of this study was to determine the effect of crystallinity on the corrosion behavior of the SAM 2X5 composite. Therefore, the Echem software was setup to obtain the corrosion rate of each sample. The spectrum measured the corrosion rate in mils per year (mpy) and plotted the data against the scanning time in minutes on the x-axis.

Each run lasted for 20 minutes where the samples were exposed to a minimum voltage of 3 V and a maximum of 12 V. For each of the four SAM discs, the spectrum was collected three times and an average value was used to determine the corrosion

behavior of the material. The same disc was used to complete the three runs for each sample but was polished at the beginning of each run to remove the corroded surface formed during pervious runs.

The first sample, NQ # 1, was sintered at 630°C with a 20 wt.% percent crystallinity and a total average corrosion rate that was equal to 6.91 mpy based on the results of the three runs. During the first run, the corrosion rate started at a high value of 6.32 mpy, went down to 4.10 mpy and back up to 5.80 mpy with an average value of 5.40 mpy. Higher values were observed during the second run ranging from 7.9 mpy to 7 mpy with an average value of 7.50 mpy. Similarly, the data collected during the third run had values that ranged from 7.50 mpy to 8.50 mpy with an average value of 7.84 mpy. These results are based on the data collected from the electrochemical spectra in figure 23.

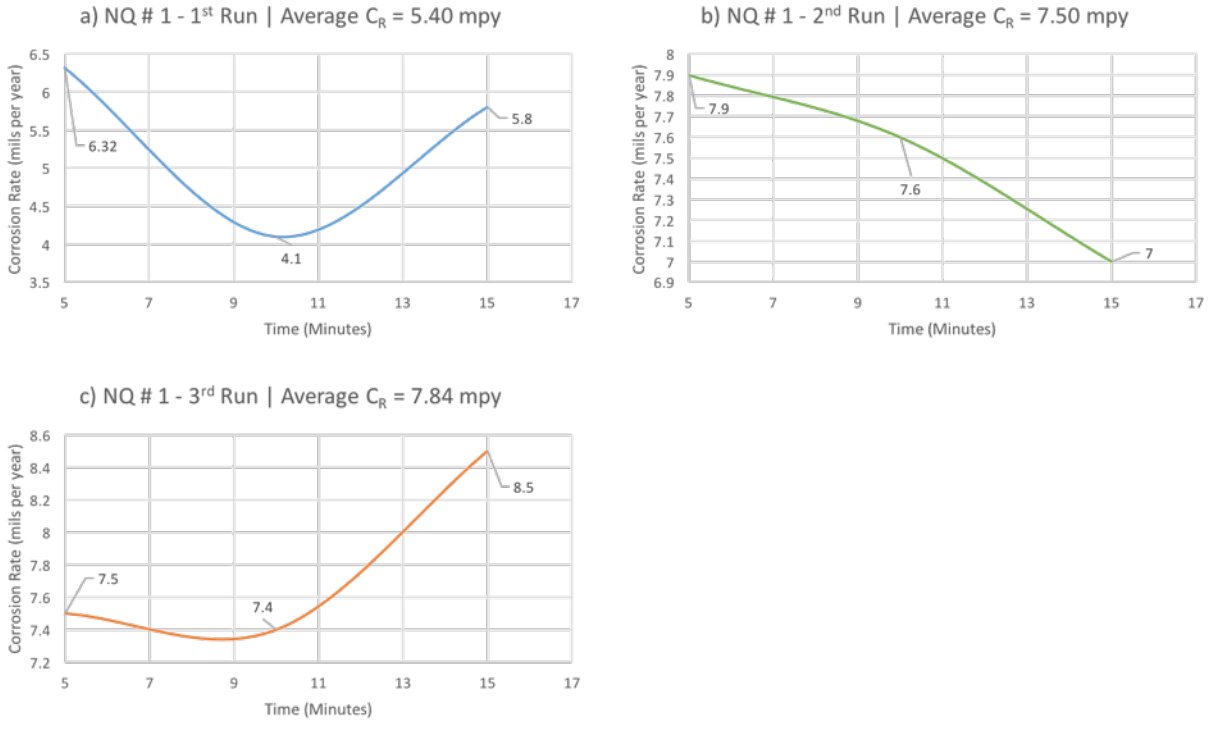

Figure 23. Results of the corrosion rate analysis of NQ # 1; (a) first run, (b) second run and (c) third run.

Additionally, the results were summarized in table 4 along with the calculated standard deviation and error. These results were also used to plot the average corrosion rate values collected during the three experimental runs for disc NQ # 1 as seen in figure 24.

Table 4. The corrosion rate values collected during the three experiments for NQ #1 along with the average values, standard deviations and errors.

Run Number	$C_{R\,1}$ (mpy)	$C_{R\,2}$ (mpy)	C_{R3} (mpy)	Average C_R (mpy)	STD	STE
Run # 1	6.32	7.9	7.5	5.4	1.16	0.67
Run # 2	4.10	7.6	7.4	7.5	0.46	0.26
Run # 3	5.80	7	8.5	7.8	0.61	0.35

The three corrosion rate data points were collected at equal time intervals during the 20 minute experimental run at 5, 10 and 15 minutes.

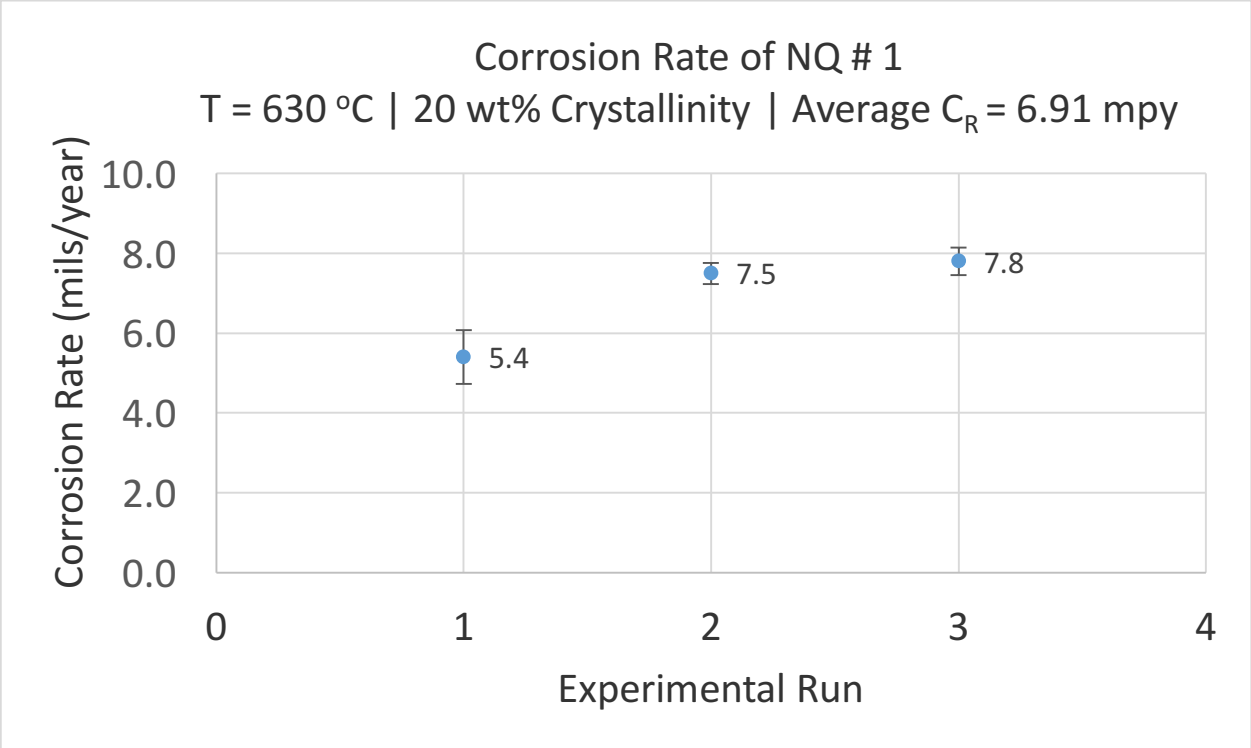

Figure 24. The corrosion behavior of disc NQ #1 during multiple experimental runs.

The inconsistent corrosion rate trends observed during the three experimental runs were caused by the structural complexity of the SAM 2X5 composite. As stated previously in section 2, when corrosion takes places on the surface of a metallic material, it results in the formation of a metal oxide. The driving force of the corrosion reaction is the Gibbs free energy of formation (ΔG_f in KJ/mol) of the metal oxide. From Thermodynamics, it is known that oxides become more stable when the value of ΔG_f becomes smaller. Therefore, oxides with a smaller ΔG_f value form more readily than oxides with higher ΔG_f values making the corrosion reaction more thermodynamically favorable.

This means that oxides with lower ΔG_f will experience a higher corrosion rate than other oxides that could potential form on the surface of the corroded metal. By applying this concept to the surface of the SAM disc which is composed of 8 different elements, multiple oxides can form when exposed to a corrosive environment. These oxides are listed in table 5 along with ΔG_f values in KJ/mol.

Table 5. The Gibbs free energy of formation of the multiple metal oxides that can form on the surface of the SAM disc when exposed to a corrosive environment [54].

Oxide	$\boldsymbol{\Delta G_f}$ **(KJ/mol)**
CoO	-214.2
MnO	-362.9
MnO_2	-465.2
WO_2	-540
MoO_3	-668.0
Fe_2O_3	-741

Based on the data listed in table 5, the oxides with the lowest ΔG_f values and the highest corrosion rates are Fe_2O_3 and MoO_3. The tungsten trioxide (WO_2) has an intermediate value and is reflected on its corrosion rate as well. Manganese and Cobalt have the highest ΔG_f values and therefore should have the lowest corrosion rate values.

With this is mind and after the sintering process, the surface of the SAM disc will contain varying compositions of these 8 different elements with unequal distributions. Therefore, when the disc is exposed to a corrosive environment, each of the elements present on the tested surface will react differently to the current as it passes through the sample based on the ΔG_f values. This thermodynamic effect explains why the data collected from the electrochemical spectra were inconsistent during a single run of the SAM disc that was being tested. When the corrosion rate was very high, it indicates that the current is passing through a part of the surface this is rich in Fe and Mo. However, lower corrosion rate values indicate that the current is passing through parts of the surface that are rich in Co or Mn. Additionally, intermediate values indicate that the current is passing through a tungsten rich part of the surface.

Despite using the same SAM disc to complete all three runs of the experiment, different trends were observed and this is because the surface of the tested disc was polished at the beginning of each run. Polishing the surface was necessary to remove corroded products from the previous run. However, polishing the sample results in exposing a new layer of the SAM disc which has a different composition than the layer tested in the previous run. This results in generating different trends and varying total average corrosion rate values for the same SAM disc. Yet, the calculated average

values are relatively close because the sintering temperature and percent crystallinity of the disc remain unchanged. Since the same experiment is used to test the other discs, this divergence is expected to be observed with all the remaining SAM discs.

The second sample, NQ # 2, was sintered at 645^{o}C with a 42 wt.% percent crystallinity and a total average corrosion rate that was equal to 9.59 mpy based on the results of the three runs. During the first run, the result followed the theoretical trend discussed in section 2.1 and the actual corrosion rate was equal to 9.80 mpy. The second run diverged from the theoretical trend and a decreasing corrosion rate was observed starting with a value of 11.20 mpy followed by 10.30 mpy and 10 mpy with an average of 10.5 mpy. A decrease in the corrosion rate was also observed during the third run with values that ranged from 9.80 mpy to 7.30 mpy with an average value of 8.46 mpy. These results are based on the data collected from the electrochemical spectra in figure 25.

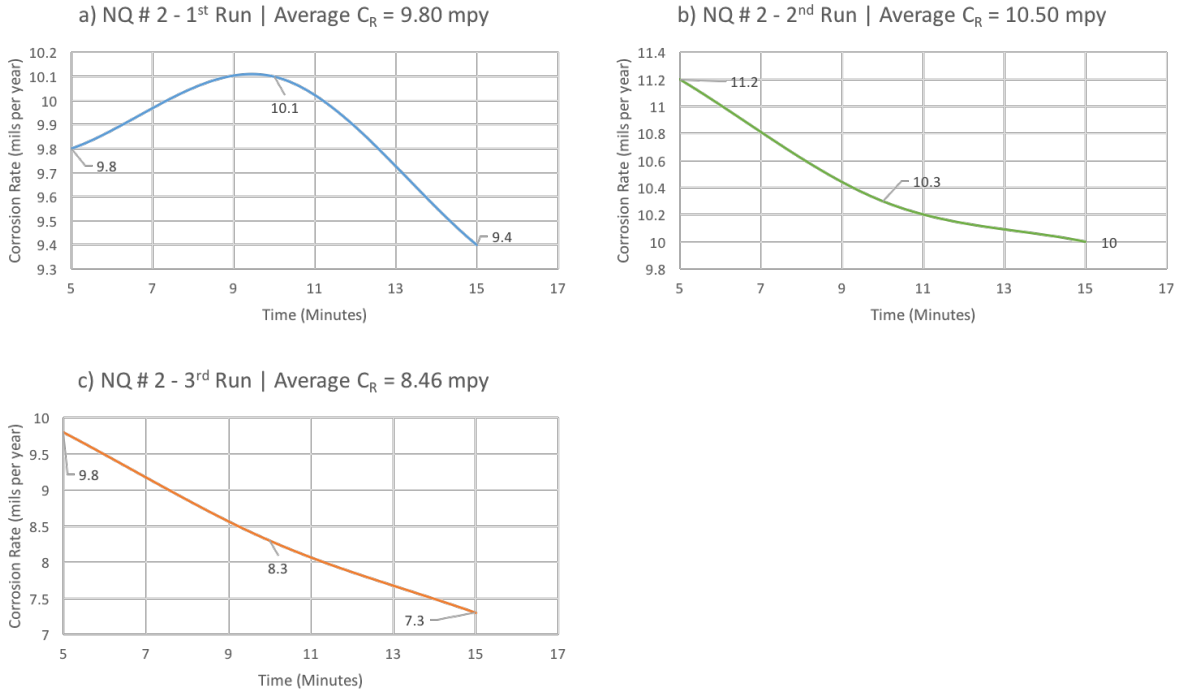

Figure 25. Results of the corrosion rate analysis of NQ # 2; (a) first run, (b) second run and (c) third run.

Additionally, the results were summarized in table 6 along with the calculated standard deviation and error. These results were also used to plot the average corrosion rate values collected during the three experimental runs for disc NQ # 2 as seen in figure 26.

Table 6. The corrosion rate values collected during the three experiments for NQ # 2 along with the average values, standard deviations and errors.

Run Number	$C_{R\,1}$ (mpy)	$C_{R\,2}$ (mpy)	C_{R3} (mpy)	Average C_R (mpy)	STD	STE
Run # 1	9.80	10.10	9.40	9.8	0.35	0.20
Run # 2	11.20	10.30	10.00	10.5	0.62	0.36
Run # 3	9.80	8.30	7.30	8.5	1.26	0.73

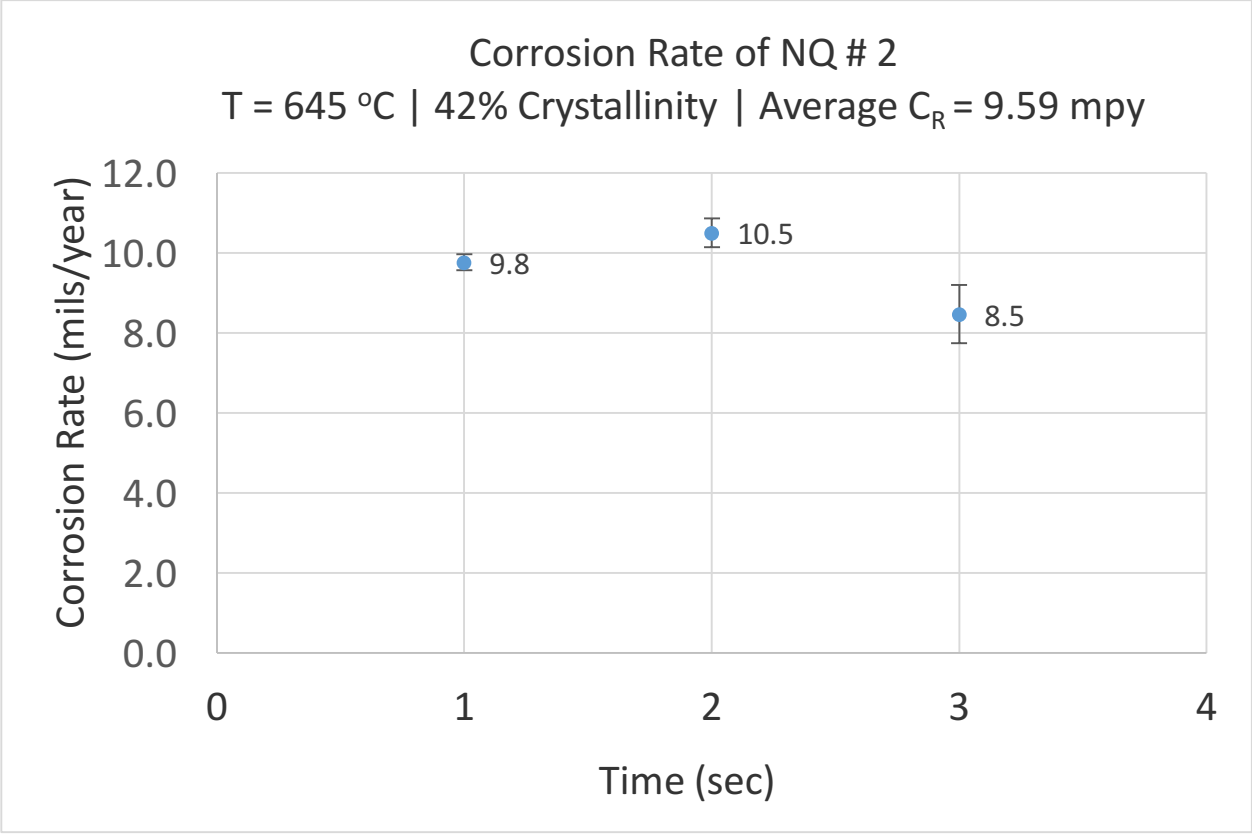

Figure 26. The corrosion behavior of disc NQ # 2 during multiple experimental runs.

The third sample, NQ # 3, was sintered at 660°C with a 61wt.% percent crystallinity and an average corrosion rate that was equal to 10.73 mpy based on the results of the three runs. A decreasing trend was observed during the first run starting with a corrosion rate of 11.60 mpy followed by 10.80 mpy and 8.20 mpy with an average of 10.2 mpy. During the second run the results fluctuated from a high value of 15.20 mpy to a very low value of 9.50 mpy and then back up to 13.00 mpy with an average of 12.6 mpy. Similarly, during the third run corrosion rate values oscillated from high to low starting with a value of 11.00 mpy, down to 5.90 mpy and back up to 11.40 mpy resulting in an average value of 9.4 mpy. These results are based on the data collected from the electrochemical spectra in figure 27.

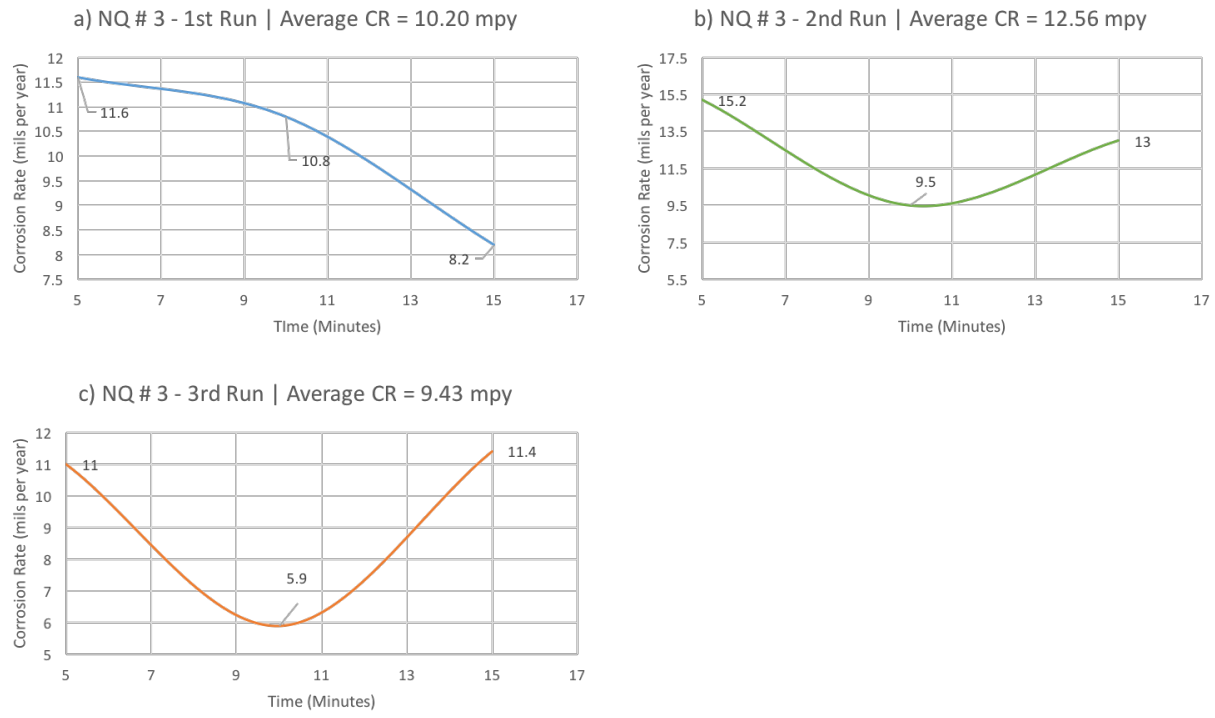

Figure 27. Results of the corrosion rate analysis of NQ # 3; (a) first run, (b) second run and (c) third run.

Additionally, the results were summarized in table 7 along with the calculated standard deviation and error. These results were also used to plot the average corrosion rate values collected during the three experimental runs for disc NQ # 3 as seen in figure 28.

Table 7. The corrosion rate values collected during the three experiments for NQ # 3 along with the average values, standard deviations and errors.

Run Number	$C_{R\,1}$ (mpy)	$C_{R\,2}$ (mpy)	C_{R3} (mpy)	Average C_R (mpy)	STD	STE
Run # 1	11.6	10.80	8.20	10.2	1.78	1.03
Run # 2	15.20	9.50	13.00	12.6	2.87	1.66
Run # 3	11.00	5.90	11.40	9.4	3.07	1.77

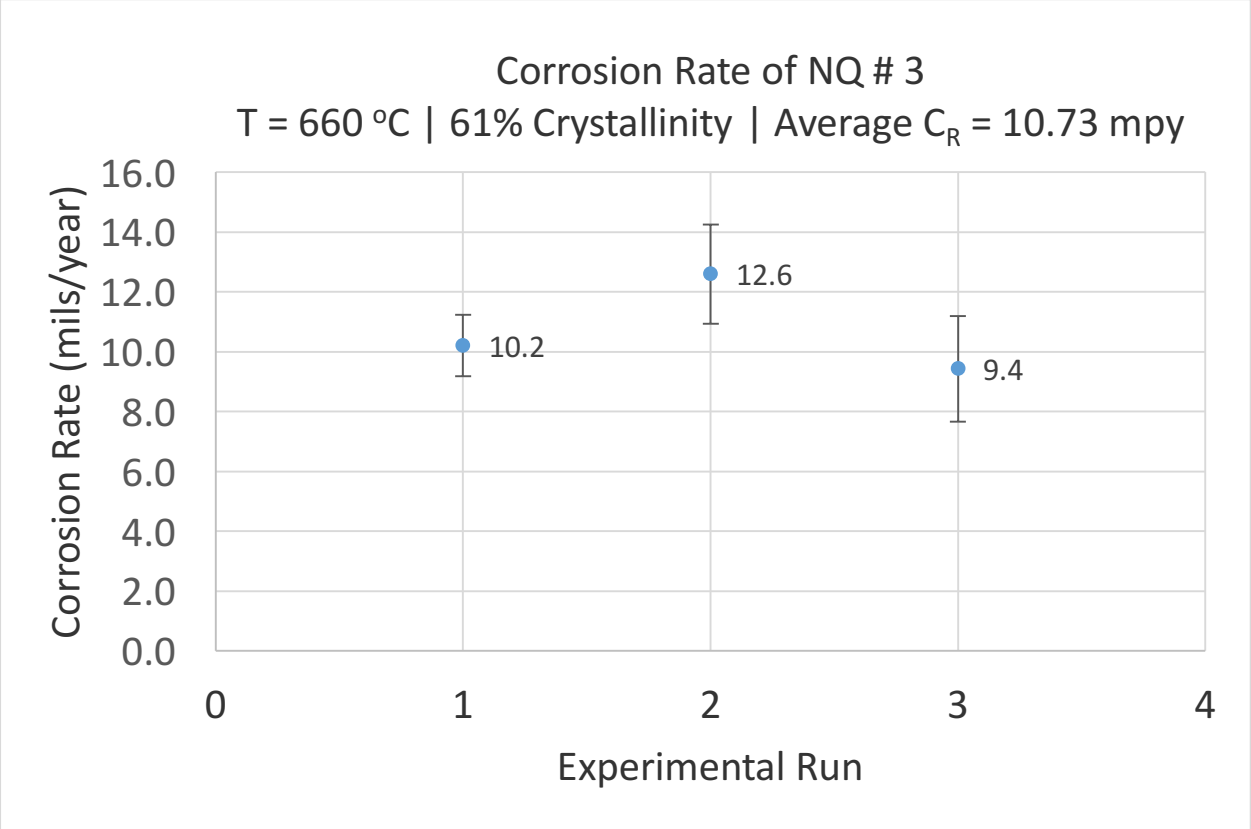

Figure 28. The corrosion behavior of disc NQ # 3 during multiple experimental runs.

The calculated standard deviation values are significantly high due to the fluctuation of the data collected during each run. This is caused by the high percent crystallinity of the sample which added a second layer of complexity to the surface of the tested disc by creating more boundaries between the crystalline and amorphous regions in addition to the thermodynamic and polishing effects discussed earlier.

The fourth and final sample, NQ # 4, was sintered at 675^{o}C with an 82 wt.% percent crystallinity and an average corrosion rate that was equal to 13.01 mpy based on the results of the three runs. During the first run, the corrosion rate was very low starting at a value of 4.2 mpy, then it went up to 16 mpy and back down to 13.5 mpy with an average value of 11.2 mpy. Data collected during the second run fluctuated in the opposite direction starting with a high corrosion rate at a value of 16.5 mpy followed by 13.00 mpy and 13.50 mpy with an average value of 14.3 mpy. Similar to the first run, the corrosion rate of the third run started at low value of 12.80 mpy, then went up to 13.90 mpy and back down to 13.70 mpy with an average corrosion rate of 13.46 mpy. These results were based on the data collected from the electrochemical spectra in figure 29.

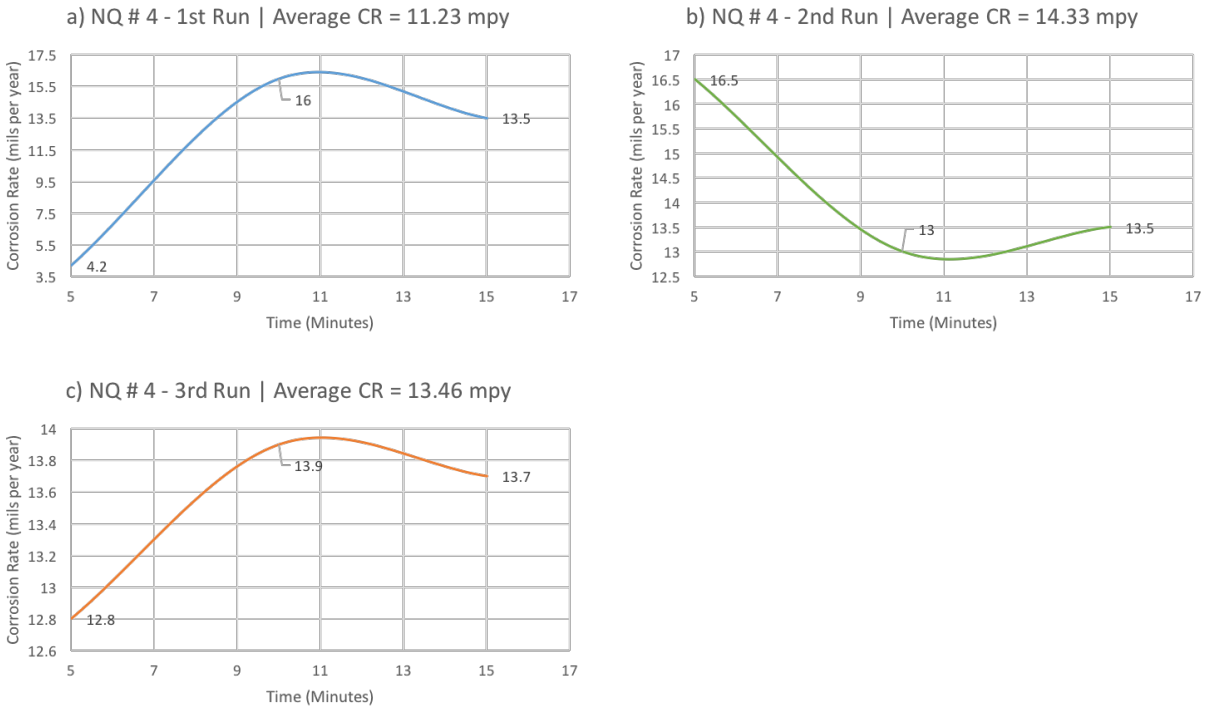

Figure 29. Results of the corrosion rate analysis of NQ # 4; (a) first run, (b) second run and (c) third run.

Additionally, the results were summarized in table 8 along with the calculated standard deviation and error. These results were also used to plot the average corrosion rate values collected during the three experimental runs for disc NQ # 4 as seen in figure 30.

Table 8. The corrosion rate values collected during the three experiments for NQ # 4 along with the average values, standard deviations and errors.

Run Number	$C_{R\,1}$ (mpy)	$C_{R\,2}$ (mpy)	C_{R3} (mpy)	Average C_R (mpy)	STD	STE
Run # 1	4.20	16.00	13.50	11.2	6.22	3.59
Run # 2	16.50	13.00	13.50	14.3	1.89	1.09
Run # 3	12.80	13.90	13.70	13.5	0.59	0.34

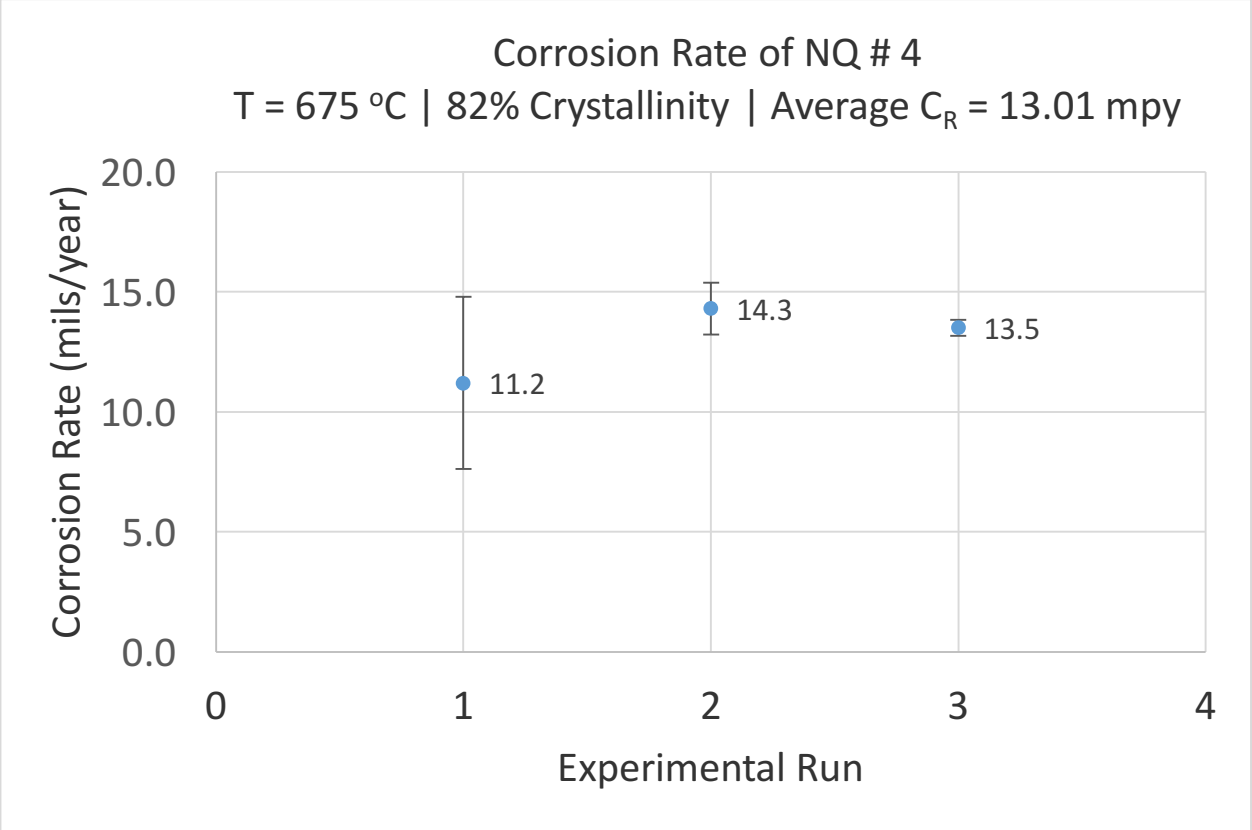

Figure 30. The corrosion behavior of disc NQ # 4 during multiple experimental runs.

It is important to note that in addition to the structural complexity of the SAM 2X5 composite and the polishing effect, the instrument used to complete this experiment is designed for a sample that is 2 cm in width and 5 cm in length. Therefore, the utilization of a copper wire to accommodate the small sample size of the SAM 2X5 disc contributed to the inconsistent trends observed in the electrochemical spectra. Nevertheless, the results of the twelve experiments were summarized in table 9.

Table 9. The various SAM disc samples along with their sintering temperatures, percent crystallinity and experimentally calculated corrosion rate measured during three different runs.

Code	Temperature (°C)	Percent Crystallinity (%)	C_R (mpy) 1 Run	C_R (mpy) 2 Run	C_R (mpy) 3 Run
NQ # 1	630	20	5.40	7.50	7.84
NQ # 2	645	42	9.80	10.50	8.46
NQ # 3	660	61	10.20	12.56	9.43
NQ # 4	675	82	11.23	14.33	13.46

Additionally, the average values of the corrosion rates were calculated for the three runs of each sample along with the standard deviation and standard error using Excel with the summarized results listed in table 10.

Table 10. The various SAM disc samples along with their percent crystallinity, calculated average corrosion rate measured during three different runs, the standard deviation and standard error.

Code	Percent Crystallinity (%)	Average C_R (mpy)	STD	STE
NQ # 1	20	6.91	1.32	0.76
NQ # 2	42	9.59	1.04	0.60
NQ # 3	61	10.73	1.63	0.94
NQ # 4	82	13.01	1.60	0.92

To gain a comprehensive understating of how the corrosion behavior of the SAM 2X5 composite was affected by the percent crystallinity, the data in table 10 were used to generate a plot of the average corrosion rates versus the percent crystallinity illustrated in figure 31.

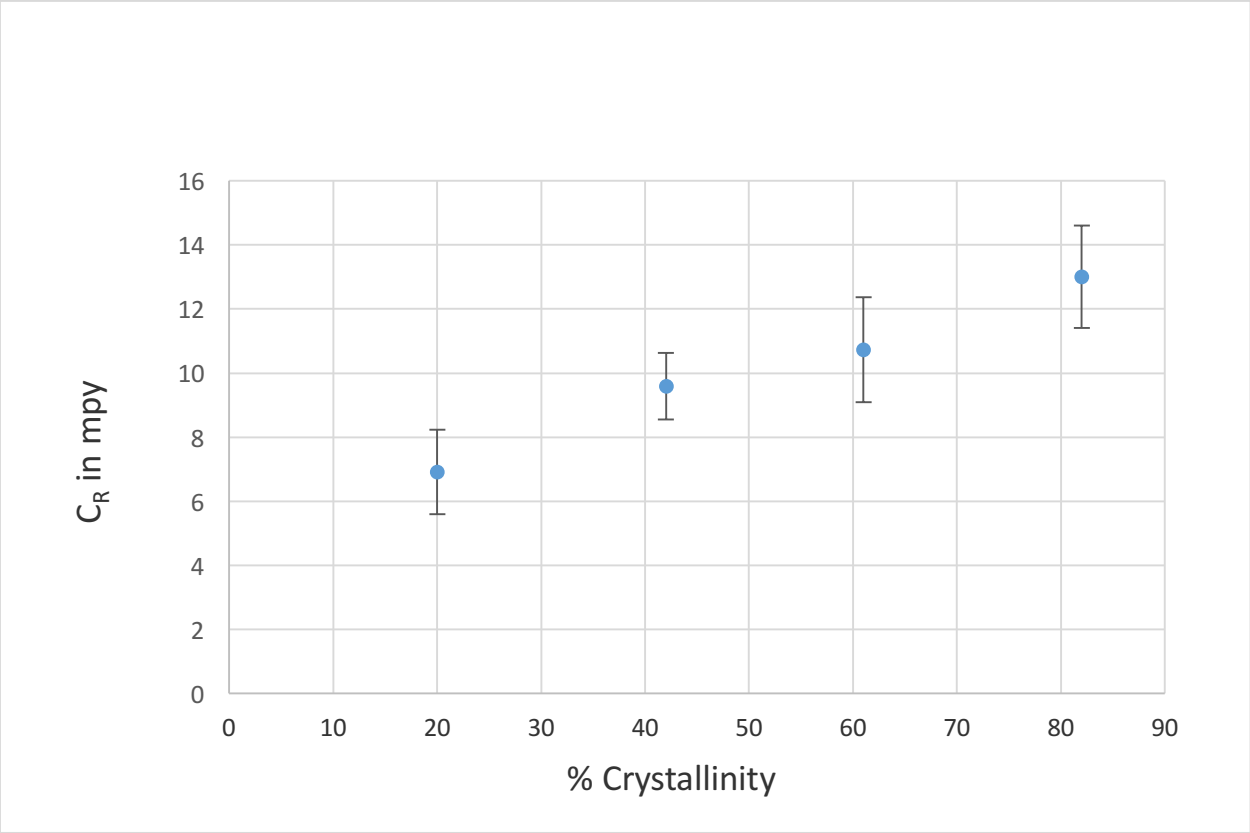

Figure 31. Average corrosion rate of SAM discs vs. percent crystallinity based on data shown in table 2 which were collected during three experimental runs for each sample.

Experimental results suggest a linear relationship between percent crystallinity and the corrosion rate, where an increase in the percent crystallinity resulted in increasing the corrosion rate of the SAM 2X5 composite. Since higher temperatures result in increasing the crystallization rate of the SAM 2X5 composite, it can be concluded that the SAM 2X5 composite has the highest ability to resist corrosion at 6.91 mpy when sintered at 630 ^{o}C with a 20 wt.% crystallinity.

Section 5. Microstructural Analysis

As stated previously, sample size adjustments and structural complexity resulted in generating inconsistent trends during the electrochemical analysis. Each one of eight

different elements responded differently to the passage of current in the sample during the corrosion testing. Therefore, scanning electron microscopy (SEM) was used to gain a better understating of the corrosion mechanism taking place on the surface of the SAM 2X5 composite and to confirm the thermodynamic effect.

First, SEM images of the pre-corroded polished SAM 2X5 disc were taken as seen in figure 32.

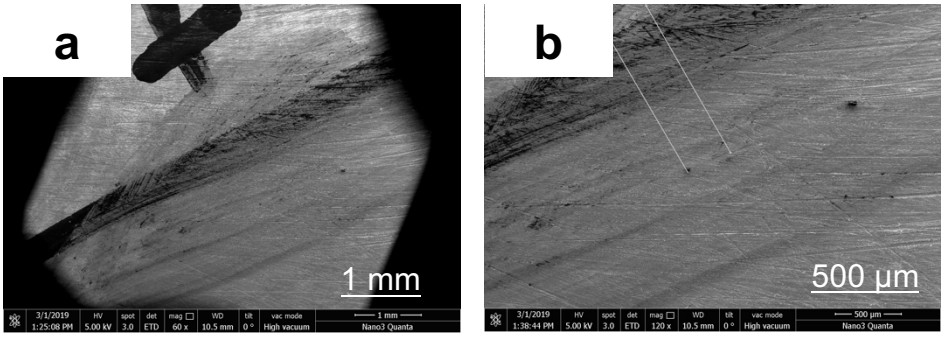

Figure 32. SEM images of the pre-corroded polished surface of the SAM 2X5 disc at different magnifications.

The disc was immersed in a 3.5 vol.% salt solution for 8 days and SEM images of the corroded surface were taken (figure 33) based on the location specified in figure 32.

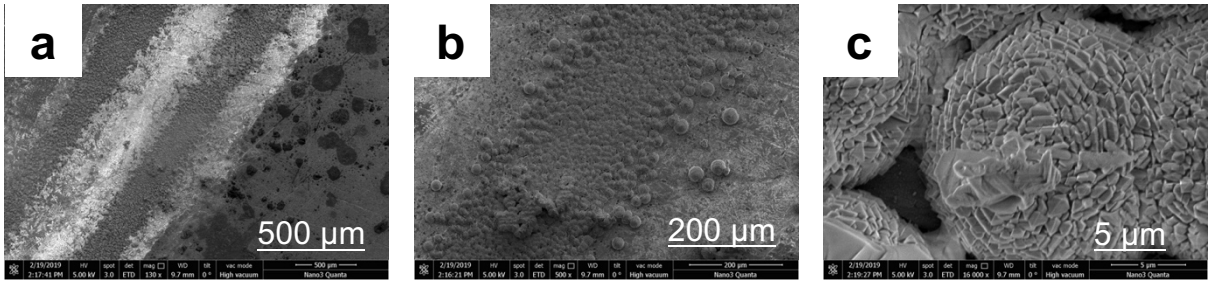

Figure 33. SEM images of the corroded SAM 2X5 disc at different magnifications.

By taking a closer look into the corroded surface, it was observed that corrosion was taking place along the boundaries between the crystalline and amorphous regions of the disc as seen in figure 34.c. This confirms that intergranular localized corrosion is attacking the boundaries on the surface of the SAM disc where parts of surface are suffering from severe corrosion while other parts remain unaffected.

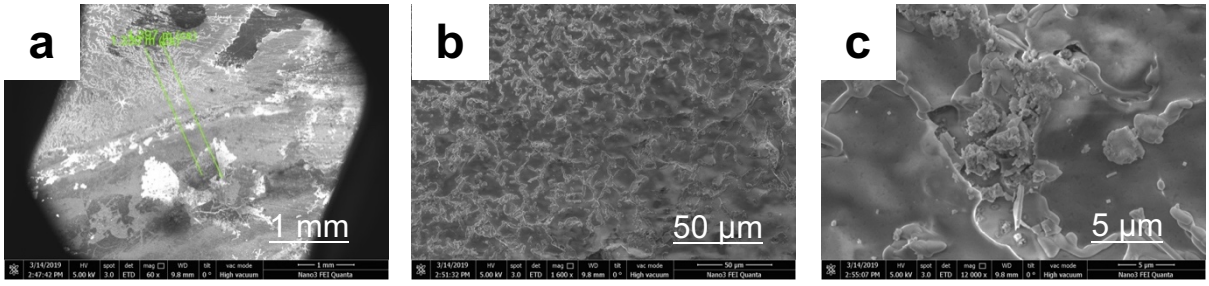

Figure 34. SEM images of a specified location on the corroded surface of the SAM 2X5 disc at different magnifications.

Additionally, different corrosion patterns were observed when scanning other locations along the corroded surface. The SEM images seen in figure 35 confirm that the compositional elements of the SAM 2X5 composite were responding differently to the current as it passes through the sample which resulted in generating three different patterns on the same corroded surface.

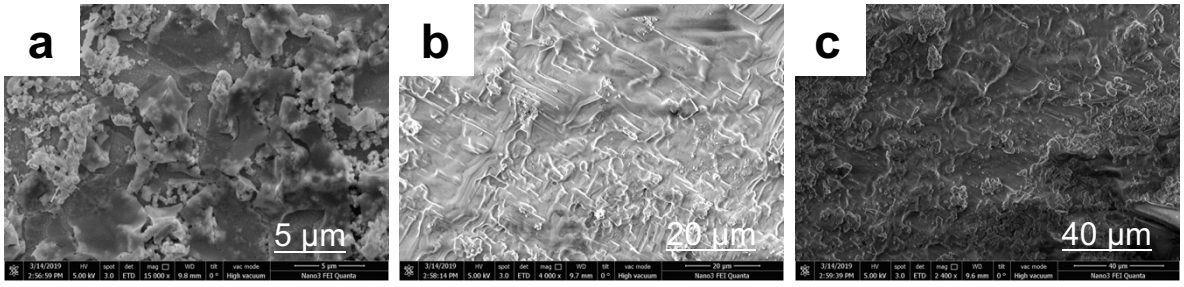

Figure 35. SEM images of multiple locations on the surface of the corroded surface of the SAM 2X5 disc showing different corrosion patters at different magnifications.

Furthermore, the corroded surface was used to develop an elemental map and it was found that the composition of the corroded surface included B, C, Mn, Fe, Cu and Co along with O, Na and Cl. The first six elements belong to the SAM 2X5 composite and the appearance of Cu was due to the utilization of a copper wire when connecting the sample to the corrosion test cell. The presences of Na and Cl were due to the immersion of the sample in a salt solution. The appearance of oxygen in the map confirms the formation of metallic oxides on the surface as a result of corrosion.

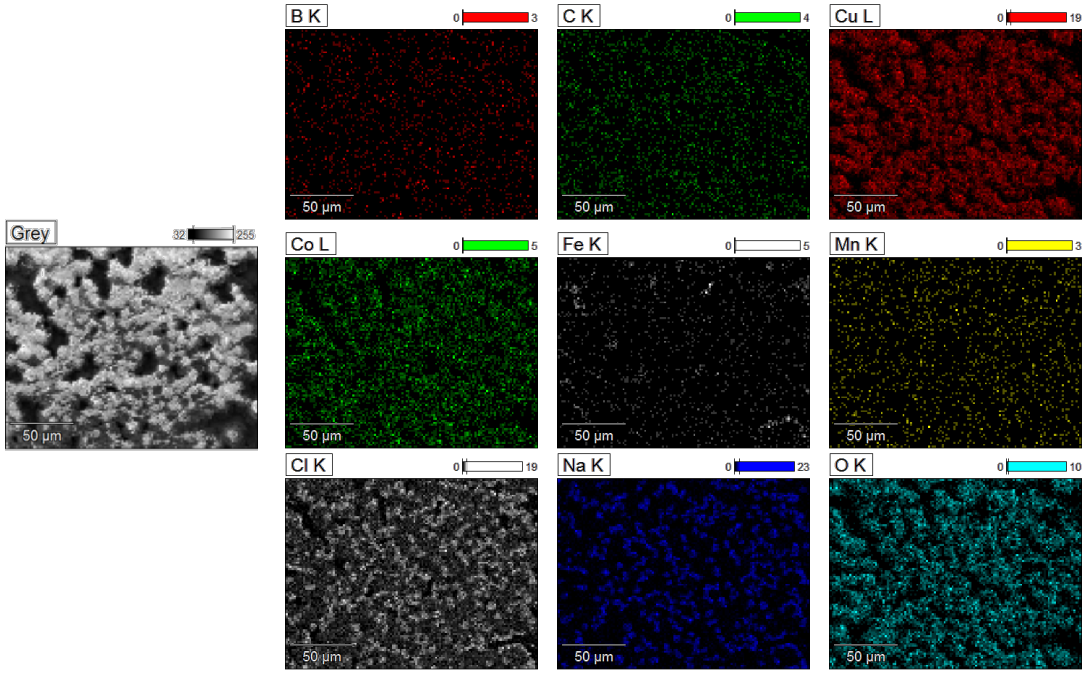

Figure 36. Elemental mapping of the corroded area confirming the presence of the SAM 2X5 composite elements along with Sodium (Na), Chlorine (Cl) and Oxygen (O) as a result of the corrosion reaction.

Due to the presence of four different metals, multiple metallic oxides can form and the Gibbs free energy values were used to determine the identity of the metallic oxides. As stated previously, the smaller the value of the Gibbs free energy, the more stable the oxide is and based on the values collected from standard thermodynamic

tables [54], the predominate oxide was identified as Iron oxide. This outcome is expected given that the SAM 2X5 composite is composed of 49% iron.

Table 11. The values of the formation energy of the various oxides that were used to identify the predominate oxide [54].

Oxide	ΔG_f **(KJ/mol)**
Fe_2O_3	-741
MnO_2	-465.2
MnO	-362.9
CuO	-129.7
CoO	-214.2

To further confirm the results of the elemental mapping, Energy Dispersive X-ray Spectroscopy (EDX) was used to determine the distribution of elements on the corroded surface. Sharp peaks appeared with high intensity for Fe, C, Mn, B, Cu, Co and Cl as seen in figure 37 which was consistent with the elemental map results. The peak with the highest intensity was identified with iron and oxygen which further confirms the identity of the metal oxide formed on the surface of the disc as iron oxide. Also, the sharp intense peak identified the presences of Manganese and oxygen on the surface indicating the formation of Manganese dioxide on the corroded surface as well.

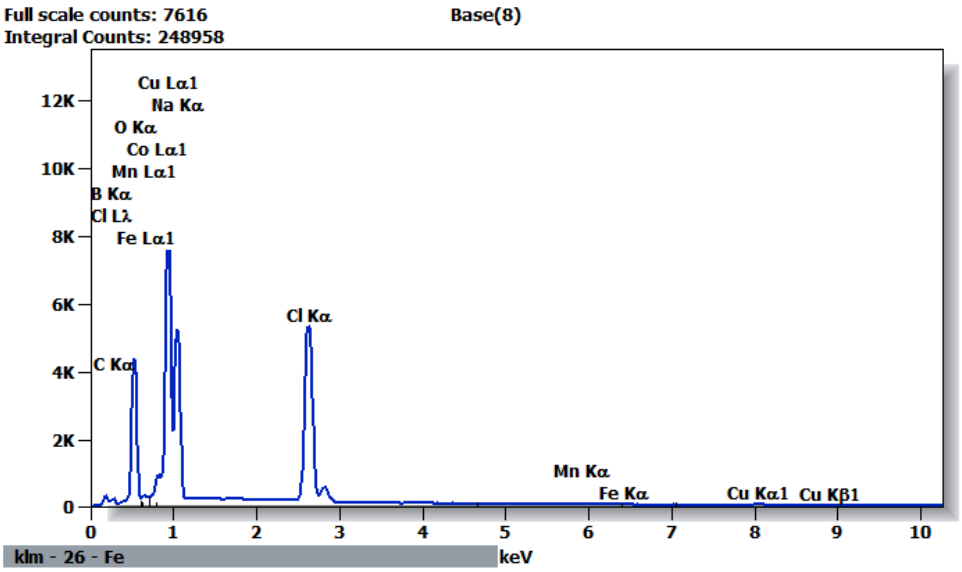

Figure 37. The EDX spectrum collected by scanning the corroded surface of the SAM disc.

By completing the microstructural analysis, it was confirmed that localized intergranular corrosion was attacking the boundary between the crystalline and amorphous phases on the surface of the SAM disc. This confirmed that an increase in the percent crystallinity generated more boundaries on the surface creating an ideal environment for corrosion. This caused an increase in the corrosion rate as observed from the results of the electrochemical analysis. Additionally, a deeper insight was gained into how the different elements in the SAM 2X5 composite behave in a corrosive environment and SEM images confirmed that multiple corrosion mechanisms were taking place on the surface of the corroded disc. Finally, the elemental map and EDX spectrum were used to identify the elements present on the corroded surface of the disc including the compositional elements of the SAM 2X5 composite, salt, iron oxide and

manganese dioxide which are products of the corrosion reaction taking place on the surface.

Section 6. Industrial Application, The Coronado Bridge

6.1 Business Case

The Coronado Bridge connects the city of San Diego to the Island of Coronado, California via the San Diego Bay. The bridge is 11,179 feet long and 63 feet wide. It took two years to construct the bridge from 1967 to 1969 and was built using pre-stressed concrete and stainless-steel [55].

Although it is one of San Diego's remarkable landmarks, it is also known to be one of the most-often used bridge for suicide in the United States. In fact, as of February 2019 more than 420 deaths were reported since the bridge became operational in 1969 [56]. Preventive measures such as the installation of nets, fences and glass barriers have been adopted. More recently, during the first quarter of 2019, 1.2 mils of stainless-steel spikes were installed on both sides of the bridge at cost of $300,000 illustrated in figure 38 below [56].

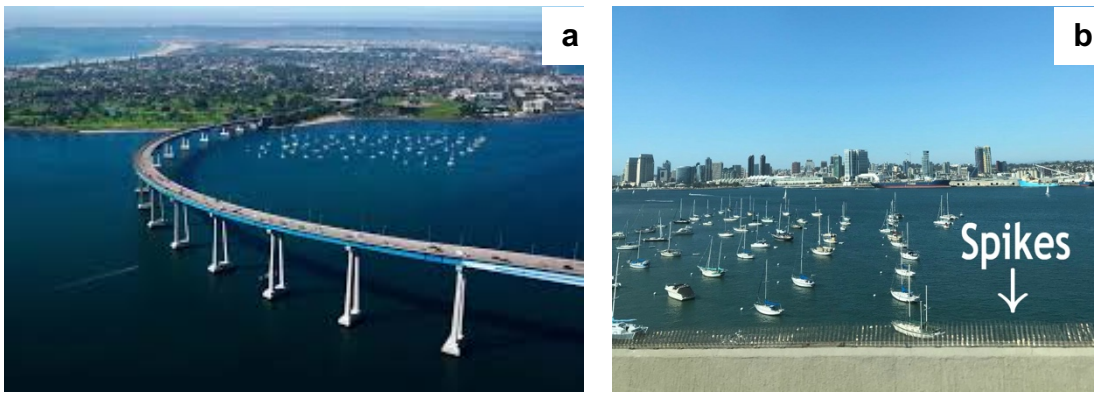

Figure 38. San Diego's Coronado Bridge (a) and the preventive stainless-steel spikes that were installed on both side of bridge during the first quarter of 2019 (b). [56]

Due to the location of the spikes, they are exposed to a highly saline and corrosive environment which was an opportunity to test the performance of the SAM 2X5 composite as a metallic coating in an industrial application to protect the stainless-steel spikes from corrosion and cut maintenance costs by increasing the service life of the spikes.

6.2 Application and Microstructural Analysis

Using High-Velocity Oxygen Fuel (HVOF), the SAM 2X5 composite was used to coat multiple spikes on the bridge. The coating was applied in March of 2019 by a third-party vendor and was monitored with comparison to the uncoated stainless-steel spikes for four months using corrosion rate analysis and SEM imaging.

Before completing the corrosion rate analysis, SEM images were taken of the coated surface to evaluate its quality. As seen in figure 39, the surface of the coating is highly porous and rough. The high porosity allows the salty bay water to penetrate the surface and will result in reducing the service life of the coating as will be confirmed by the corrosion rate analysis.

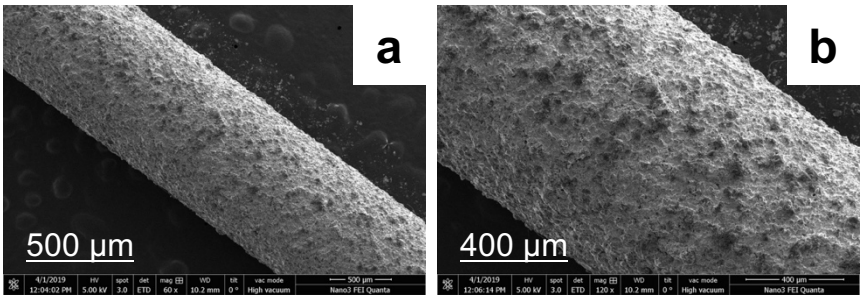

Figure 39. SEM images of the SAM 2X5 coated stainless-steel surface at different magnifications.

In order to complete the corrosion rate analysis, it was necessary to determine the thickness of the coating. This was done by taking a cross-sectional SEM image of the sample which was imbedded in PELCO epoxy and polished as stated in section 4. It was found that the thickness of the coating ranged from 84.99 to 97.11 μm with an average value of 92.37μm based on the data shown in figure 40.

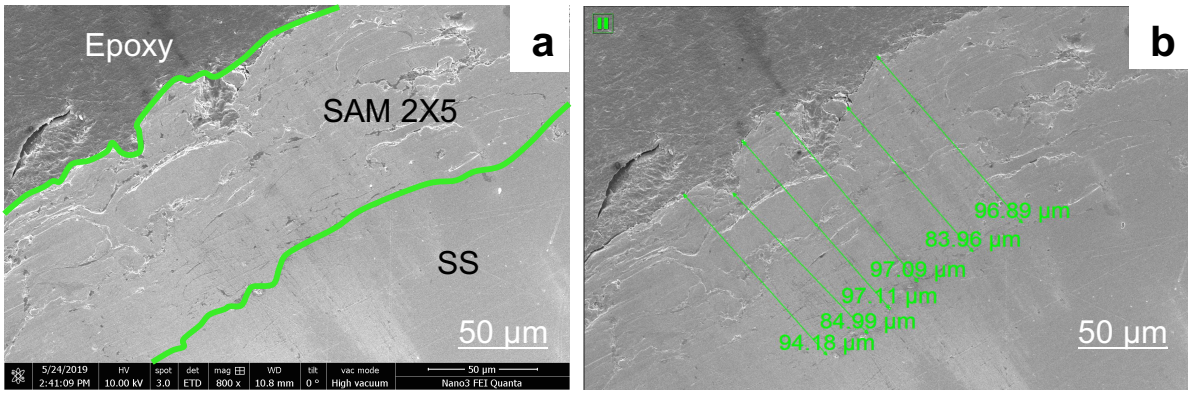

Figure 40. Cross sectional SEM images of the coated stainless-steel sample; (a) interface between the stainless-steel and the SAM coating and (b) measured thickness with an average value of 92.37 μm.

Additionally, the same SEM image shown in figure 40.a was used to collect the EDX spectrum. This was done to distinguish between the coated and uncoated area of the stainless-steel sample through chemical composition as seen in figure 41 and to confirm the calculated average thickness value of the SAM coating.

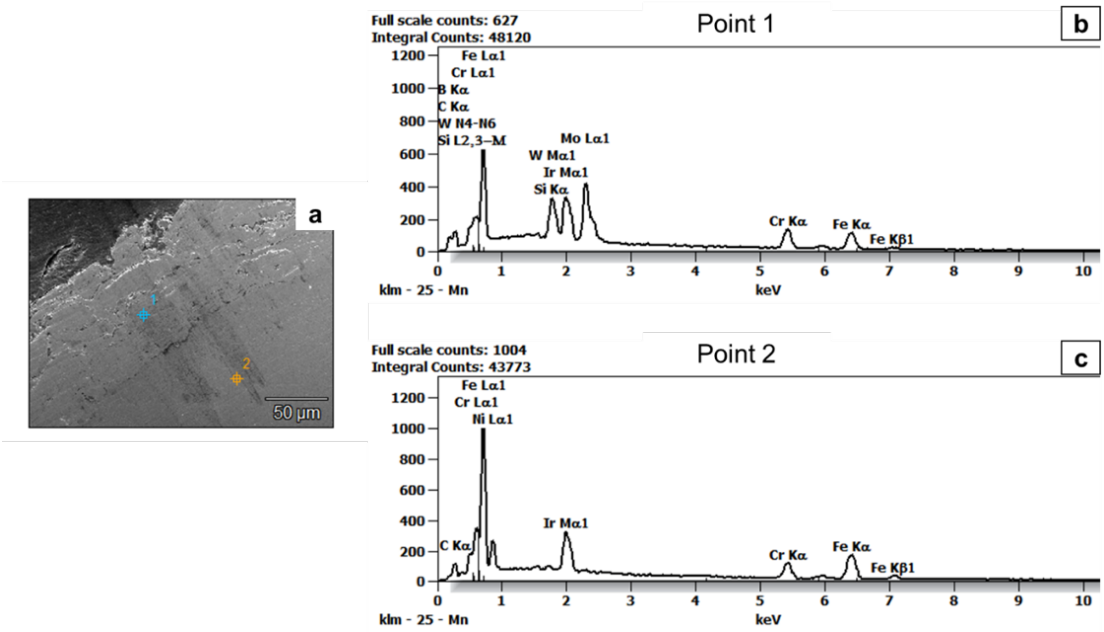

Figure 41. Results of the EDX analysis distinguishes between the chemical composition of the coated and uncoated areas of the stainless-steel sample; (a) the cross-sectional SEM image used to complete the EDX analysis, (b) EDX spectrum of the coated area and (c) EDX spectrum of the uncoated area.

6.3 Corrosion Rate Analysis

Samples were prepared using the same procedure described in section 3 and the corrosion rate analysis was completed using the same instrument, a three-electrode corrosion test cell with immersion into a 3.5 vol.% NaCl solution. For this experiment, the surfaces of the samples were not polished because the coated surface was being tested and a 15 cm copper wire was used to connect the immersed spike to the cell.

The first experimental test was completed on the pre-installed (0 Months) samples. The electrochemical spectrum of the SAM coated sample had a decreasing corrosion rate starting with a value of 14.20 mpy followed by 8.10 mpy and 7.00 mpy with an average value of 9.10 mpy. On the other hand, the uncoated stainless-steel

sample had an increasing corrosion rate trend starting with a value of 17.40 mpy followed by 21.80 mpy and 47.50 mpy with an average value of 28.9 mpy. These results were based on the data collected form the electrochemical spectra seen in figure 42.

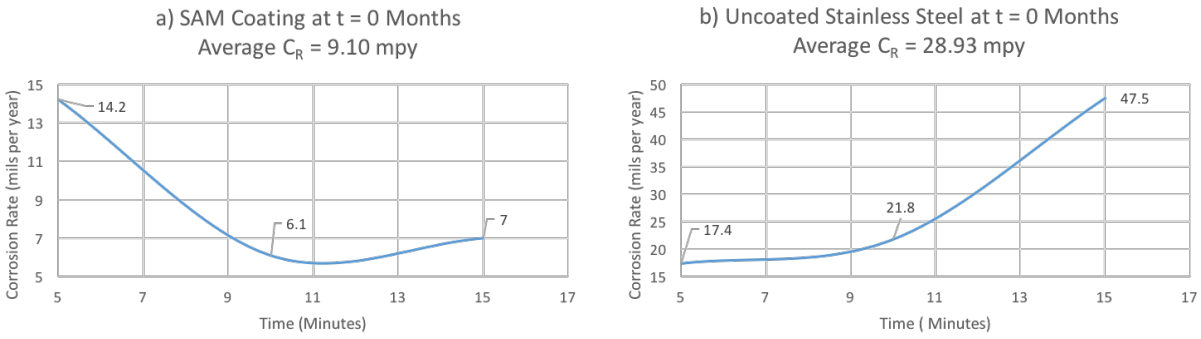

Figure 42. The corrosion rate analysis of the coated (a) and uncoated stainless-steel(b) samples measured at time = 0 Months (before installation on the Coronado Bridge).

The second experimental test was completed on samples that were brought back from the bridge after two months. The electrochemical spectrum of SAM coated samples had a slightly fluctuating trend starting at a high value of 19.40 mpy, then it went down to 12.50 mpy and back up to 12.70 mpy with an average value of 14.8 mpy. The uncoated stainless steel sample had a decreasing corrosion rate trend that started with a high value of 31.70 mpy followed by 29.30 mpy and 16.30 mpy with an average corrosion rate of 25.8 mpy. These results were based on the data collected from the electrochemical spectra seen in figure 43.

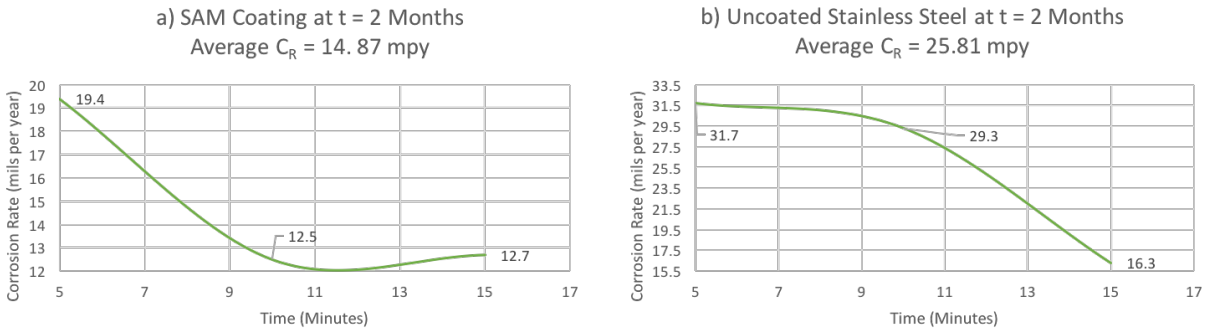

Figure 43. The corrosion rate analysis of the coated (a) and uncoated stainless-steel(b) samples measured two months after deployment on the Coronado Bridge.

The increase in average corrosion rate of the coated sample indicated that coating has suffered from initial deterioration. However, the stainless-steel sample should have maintained a constant corrosion rate but a slight decrease was observed instead. This is most likely due to an experimental error that may have occurred during the test. Similar to the observations made while testing the corrosion rate of the SAM 2X5 discs, the inconsistent trends were due to the complex structure of the the SAM coating along with the utilization of a copper wire to connect the tested sample to the cell during the experiment. Therefore, it is expected to observe these deviations in the remaining electrochemical spectra collected for the coated and uncoated samples.

The third and final experimental test was completed on samples that were brought back from the bridge after four months. This time, the corrosion rate of the SAM coating had an increasing trend starting with a value of 24.80 mpy followed by 24.10 mpy and 28.80 mpy with an average of 25.9 mpy. Similarly, the uncoated stainless steel sample had an increasing trend that started with a value of 31.80 mpy followed by a very low value of 9.1 mpy and a high value of 51.80 mpy with an average rate of 30.9

mpy. These results were based on data collected from the electrochemical spectra seen in figure 44.

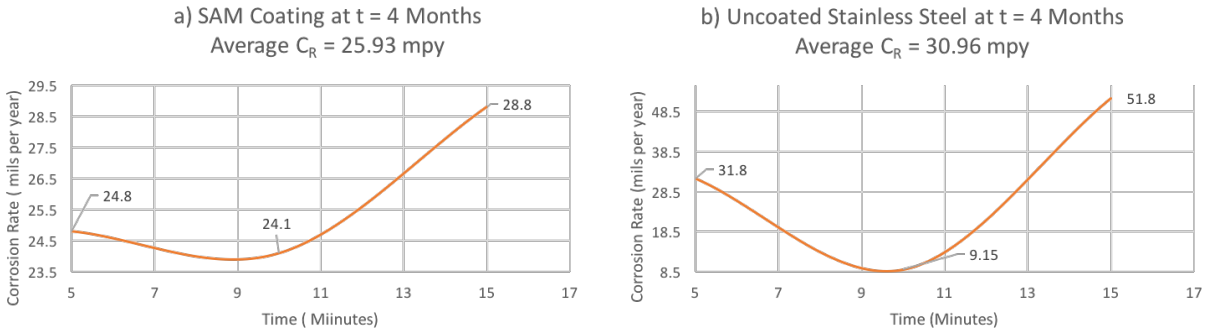

Figure 44. The corrosion rate analysis of the coated (a) and uncoated stainless-steel(b) samples measured four months after deployment on the Coronado Bridge.

The significant increase in the corrosion rate of the coated samples from a low value of 9.10 mpy to 25.93 mpy indicated the coating had suffered failure after 4 months of deployment due to the salty environment of the San Diego Bay. Based on the data collected during the four-month monitoring period, the performance of the coating was calculated based on equation 13 [57]:

$$\% \text{ Performance} = \frac{\Delta C_R}{C_R\,(\text{Stainless Steel})} \times 100 \quad \textbf{(13)}$$

Table 12 summarizes the finding along with calculated performance of the SAM coating during the four-month monitoring period and was used to generate a plot that compares the performance of the coated and uncoated samples with respect to time as seen in figure 45.

Table 12. The results obtained from the corrosion rate analysis experiments completed to monitor the performance of the SAM coating during its utilization on the Coronado Bridge.

Time	SAM Coating C_R (mpy)	Stainless-steel C_R (mpy)	Performance
0 months	9.10	28.93	66.29%
2 months	14.87	25.81	42.38%
4 months	25.93	30.96	16.24%

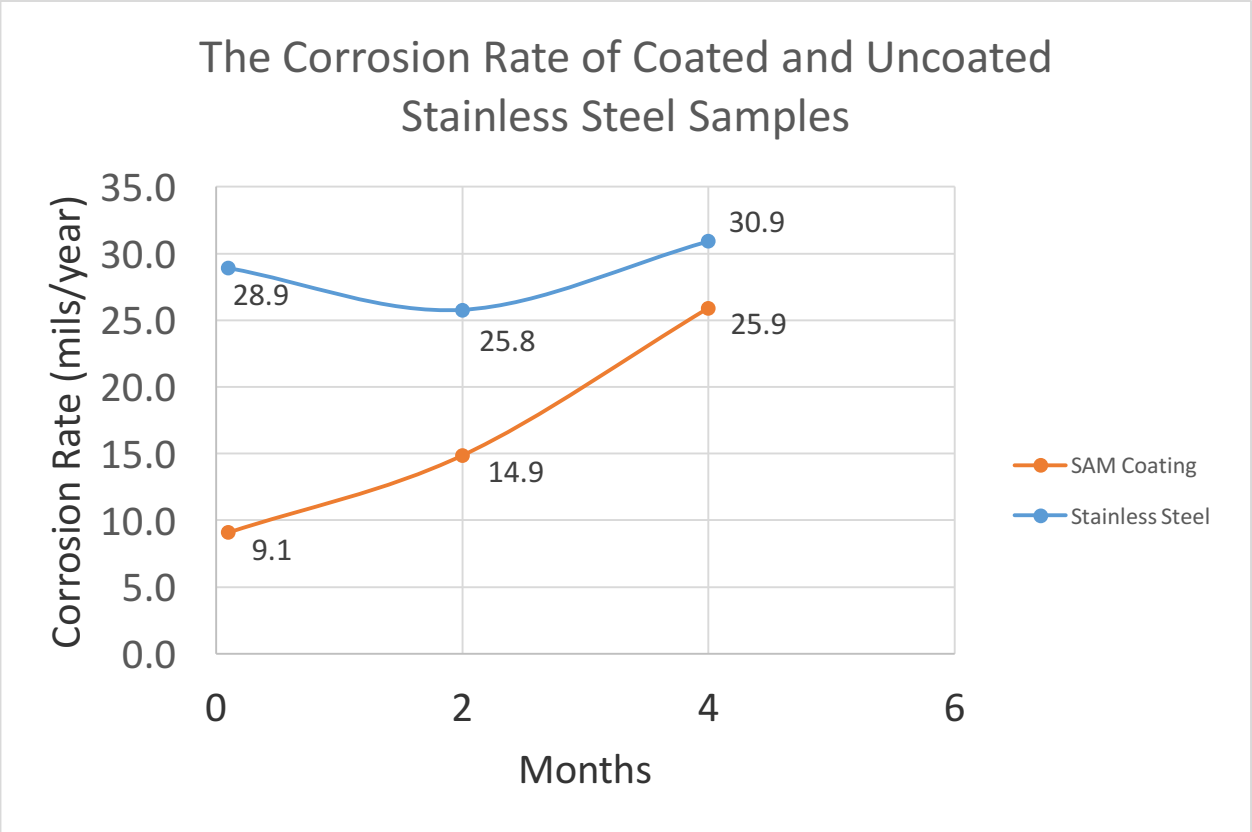

Figure 45. Compares the performance of the SAM coated spikes and the uncoated stainless-steel spikes with respect to time during the four-month monitoring period.

The results indicate that Before installation at 0 Months, the SAM coating had an average corrosion of 9.1 mpy while the uncoated sample had an average value of 28.9 mpy. After 2 Months, the coating began to deplete and its average corrosion rate went up to 14.9 mpy. However, the uncoated sample maintained a semi-constant average corrosion rate of 25.8 mpy and the reported lower value is mostly likely due to experimental error**.** At 4 Months, the coating began to deteriorate and its average corrosion rate went up to 25.9 mpy while the uncoated stainless-steel sample had a slightly higher corrosion rate of 30.9 mpy.

Theoretically, at 0 months the SAM coating outperformed stainless-steel by 66% but after two months of deployment, the performance of the coating went down to 42% due to initial depletion. At 4 months, the coating started to show signs of sever failure and its performance went down to 16%. Nevertheless, the coating had managed to increase the service life of stainless-steel by 4 months which can result in significant reductions to maintenance costs. However, this rapid deterioration of the SAM coating was unexpected and microstructural analysis was conducted in order to understand the deterioration mechanism of the SAM coating and determine the depletion rate.

6.4 Deterioration of The SAM 2X5 Coating

A comprehensive idea can be formulated about the deterioration of the coating during the 4-month period by comparing the cross-sectional images of the coated samples seen in figure 46.

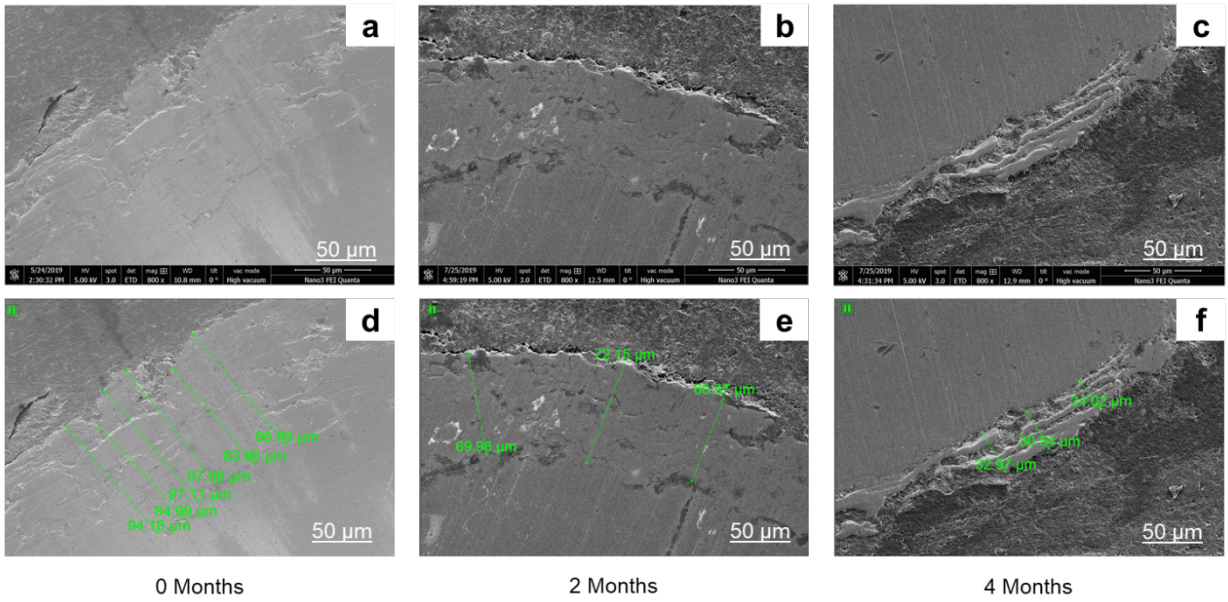

Figure 46. Cross sectional SEM images of the coated stainless-steel samples along with the associated thickness; (a)(d) at 0 months, (b)(e) at 2 months and (c)(f) at 4 months.

By analyzing the data collected from the SEM images, it was found that the SAM coating was depleting at rate of 12.35 µm per month based on the calculated average thickness of the coating listed in table 13.

Table 13. Comparing the thickness, corrosion rate and performance of the SAM coating during the 4-month monitoring period.

Parameters	**0 Months**	**2 Months**	**4 Months**
Thickness (µm)	92.37	67.66	29.17
SAM Coating C_R (mpy)	9.10	14.87	25.93
Performance	66.29%	42.38%	16.24%

Prior to installation, the SAM coating had an average thickness of 92.37 μm (figure 46.d) and showed good adhesion to the surface of the stainless-steel spike as seen from figure 46.a. After 2 months of exposure to the salty Bay environment, the thickness of the coating went down to an average value of 67.66 μm (figure 46.e). The appearance of dark areas at the interface (figure 46.b) was a sign of reduced adhesion between the two surfaces and initial deterioration of the coating. Exposure for another 2 months resulted in reducing the thickness to an average of 29.17 μm (figure 46.f) which explained why the performance of the coating rapidly decreased to 16% and its corrosion rate value was very close to that of uncoated stainless-steel.

6.5 Conclusion and Recommendations

Initial experimental results indicated that the SAM coating at 0 months had a corrosion rate of 9.10 mpy and would last 8 months longer than the uncoated stainless-steel which had an average corrosion rate of 28.83 mpy. However, corrosion rate and microstructural analysis both indicated that the coating had started to deteriorate after 2 months of deployment at a rate of 12.35 μm/month and eventually failed after 4 months of deployment. The unexpected rapid decline in the performance of the coating was primarily due to the coating application method. The HVOF technology generated a coated surface that is rough and highly porous as seen from the SEM images in figure 39. This allowed for the salty Bay water to penetrate and accelerated the deterioration rate of the coating.

Additionally, and as stated in section 1.3, the HVOF technology applies the powdered material as solid coating by melting the powder via the combustion of oxygen and kerosene. The combustion reaction takes places at temperatures that range from

2,200 to 3,000 ^{o}C which exposed the SAM 2X5 composite to extremely high temperatures. Results of the current study have shown that high temperatures directly increase the crystallinity of the SAM 2X5 composite along with its corrosion rate and its ability to resist corrosion. Therefore, it is recommended to use a different application method that does not require high operating temperatures which can maintain the SAM 2X5 composite in the amorphous state where it has the highest ability to resist corrosion.

An example of a coating technology that can be used to apply powdered materials at room temperature is known as Physical Vapor Deposition Technology commonly known as PVD coating technology. In general, the technique involves vaporizing a solid material in vacuum and depositing it on a substrate as a pure material or an alloy composite coating. The deposition process transfers the coating material on an atomic level to provide extremely pure and high performance coatings for many applications including, durable protective coatings, optical lenses, solar panels and medical devices [58,59].

There are two types of processes that are used during the coating application via PVD and they include sputtering and thermal evaporation. The sputtering process involves the bombardment of the target coating material with a high energy voltage that causes the the target material to sputter off atoms which are deposited on the surface of the substrate and this process takes place at a temperature range of 50 to 500 ^{o}C [58,59].

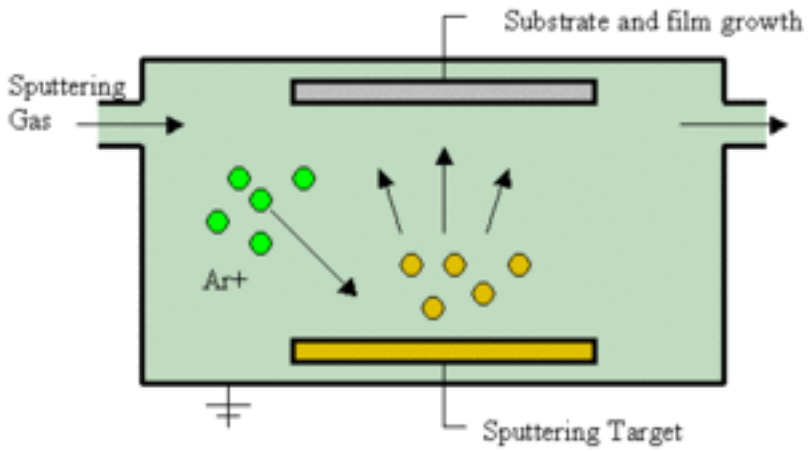

Figure 47. The working mechanism of coating a substrate using the sputtering process of physical vapor deposition [60].

On the other hand, thermal evaporation requires heating up the target coating material to its boiling point in high vacuum which results in the formation of a vapor stream of the material. Then, the high vacuum causes this vapor stream to rise in the application chamber and condense on the surface of the substrate [58].

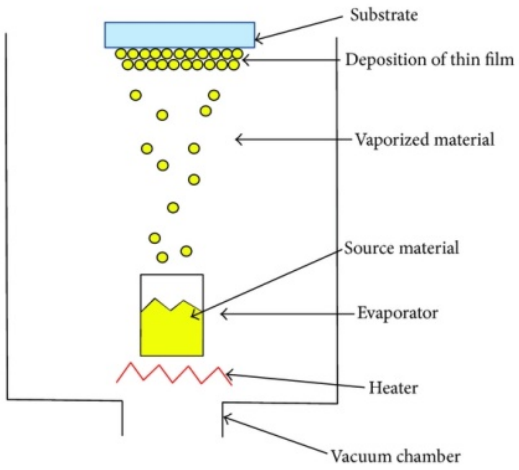

Figure 48. The working mechanism of coating a substrate using the thermal evaporation process of physical vapor deposition [61].

Based on the results of the Coronado Bridge study, it is recommended to use the sputtering process when applying the SAM coating on the surface of a substrate since it operates at the low temperatures of 50 to 500 ^{o}C which will maintain the amorphous structure of the SAM 2X5 composite along with its high ability to resist corrosion. During the sputtering process, the target coating material is placed in solid form in the application chamber [58,59]. Then, the chamber is evacuated to remove any impurities and ensure the purity of the applied coating. Once the chamber is clean, it is filled with Argon gas and a negative electric potential is applied to the target coating material [58,59].

When the electric field is applied, the target material becomes negatively charged and acts as the cathode while the chamber becomes positively charged and acts as the anode [59]. Additionally, the applied electric potential causes free electrons to accelerate away from the surface of the target material. When these free electrons collide with the Argon gas atoms, they strip them of an electron creating a positively charged gas ion [59]. The positively charged gas ion carries enough energy to sputter some of the target coating material [59]. The sputtered molecules collect on the surface of the substrate forming the desired coating [59].

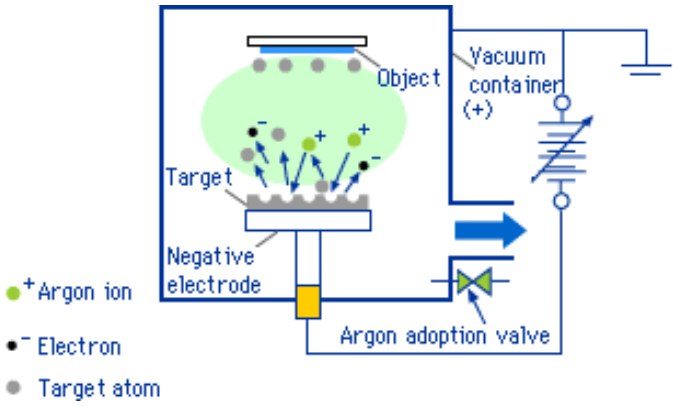

Figure 49. The application chamber used in physical vapor deposition sputtering process [62].

After that, the positively charged gas ions recombine with the free electrons in the chamber resulting in excess voltage that is released in the form of light inside the chamber [59]. Argon is commonly used as the source of the inert gas because it does not combine with the sputtered molecules of the target material and ensures that the purity of the coating is maintained throughout the application process [58,59]. Occasionally, reactive gases such as oxygen or acetylene are introduced into the chamber to create a strong bond between the coating and substrate when it is deposited [58,59]. The sputtering deposition process continues at a constant rate until the desired thickness of the coating is achieved and the power is removed from the cathode [58,59].

By using the low temperature sputtering physical vapor deposition technology to apply the SAM based coating on the surface of stainless-steel, it will most likely maintain the highly amorphous structure of the SAM 2X5 composite and prevent the formation of the crystalline phase along with the boundaries that give rise to intergranular localized corrosion on the surface of the coating. This will ensure high performance of the coating because the SAM composite is deposited in a state where it has the highest ability to resist corrosion.

Section 7. Conclusions

The objective of the current study was to determine the effect of crystallinity on corrosion behavior of an iron-based amorphous metallic alloy that is composed of $Fe_{49.7}Cr_{17.7}Mn_{1.9}Mo_{7.4}W_{1.6}B_{15.2}C_{3.8}Si_{2.4}$ and is known as the SAM 2X5 composite. Using spark plasm sintering, bulk solid samples of the SAM 2X5 powder were prepared at different temperatures ranging from 630 to 675 ^{o}C. Sintering at different temperatures resulted in increasing the weight percent crystallinity from 20 wt.% to 82 wt.%, respectively and electrochemical characterization was used to determine how the increase in crystallinity effected the corrosion behavior of the composite. An instantaneous corrosion test analysis was completed using a 1010 E Gamry potentiostat and a three-electrode corrosion test cell where samples were immersed in a 3.5 vol.% NaCl solution which served as an electrolyte and simulated a corrosive environment.

By analyzing the collected electrochemical spectra, results have shown that the corrosion rate of the SAM 2X5 discs increased from 6.91 mpy to 13.01 mpy as the percent crystallinity went up. However, the data collected from the electrochemical spectra had varying values during a single run and fluctuating corrosion rate trends during multiple runs that were completed for the same disc. The inconsistency of the experimental trends was a result of the structural complexity of the SAM 2X5 composite.

When the sample was immersed in the corrosion test cell, the current ran through the sample and the surface began to corrode by forming metal oxides. Thermodynamically, the driving force of the corrosion reaction is the formation of stable metal oxides with low Gibbs free energy of formation values. However, the surface of

the SAM 2X5 composite contained multiple elements that responded differently to the corrosion current due to the different values of Gibbs free energy of formation. Metals with lower ΔG_f such as Fe and Mo form stable oxides and have a higher corrosion rate while metals such as Co and Mn with a higher ΔG_f form less stable oxides and have a lower corrosion rate. Since these elements are distributed randomly on the surface of the SAM disc, it generated inconsistent corrosion rate values. In addition to the thermodynamic effect, the surface of the disc was polished at the beginning of each experiment which exposed a new layer of randomly distributed elements on the surface of the tested disc. Nevertheless, the collective average corrosion rate values of 4 tested discs showed an increasing trend with the percent crystallinity because the sintering temperate and percent crystallinity of each disc was kept constant throughout the experimental trials.

Microstructural analysis was used to confirm the thermodynamic effect and SEM images revealed that multiple patters of corrosion were observed on the same corroded surface indicating different responses of the multiple elements that are randomly distributed on the surface of the disc.

Additionally, it was observed that there were no significant microstructural changes in the amorphous regions of the sample and that corrosion was only taking place along the boundaries between the crystalline and amorphous regions. This confirmed that SAM 2X5 composite was suffering from localized intergranular corrosion, where the attack occurred due to the segregation of two phases and the loss of elements that are necessary for adequate corrosion protection.

Furthermore, the corroded surface was used to develop an elemental map and collect an EDX spectrum to determine the chemical identity of the compounds that formed as a result of corrosion. The five metallic elements of the SAM 2X5 composite were present in both analyses along with Sodium (Na), Chlorine (Cl) and Oxygen (O). The Na and Cl appear due to the immersion of the sample in a salt solution. While the presences of oxygen confirmed the formation of multiple metal oxides on the surface of the corroded disc.

Based on analyzing the electrochemical and microstructural analysis of the four different SAM 2X5 discs, the following conclusions can be made:

- The SAM 2X5 composite had the lowest corrosion rate when sintered at the lowest temperature where the percent crystallinity was minimized and the amorphous phase was predominating.
- The inconsistency observed in the electrochemical spectra collected during the multiple experimental runs was a result of the structural complexity of the SAM 2X5 composite.
- Two effects which influenced the results were the thermodynamic stability of metal oxides on the surface of the SAM disc and surface polishing.
- SEM images were used to confirm the thermodynamic effect along with the observation of localized intergranular corrosion attack at the boundaries between the crystalline and amorphous regions of the SAM disc

- The development of an elemental map along with collecting an EDX spectrum were used to confirm the chemical identity of the compounds formed on the corroded surface.

The development of a SAM 2X5 composite metallic coating was completed using HVOF thermal coating technology and was applied on stainless-steel spikes that were installed on San Diego's Coronado Bridge as a preventive measure to suicide. The performance of the SAM-based coating was monitored over the period of four months via instantaneous corrosion rate and microstructural analysis.

Pre-installation results showed that the coated samples had a corrosion rate of 9.10 mpy while the uncoated stainless-steel samples had a rate of 28.93 mpy indicating that the SAM 2X5 coating had the potential to outperform the uncoated stainless-steel sample by 66.29% and would increase the service life of the stainless-steel spikes by 8 months. After two months, the coating began to deplete and its corrosion rate went up to 14.87 mpy and its performance decreased to 42.38% when compared to the corrosion rate of the uncoated stainless-steel sample which was equal to 25.89 mpy. Moreover, after 4 months of deployment, the coating failed and had a corrosion rate of 25.93 mpy with a low performance of 16.24% when compared to the corrosion rate of uncoated stainless steel which was equal to 30.90 mpy.

This sharp reduction in service life was mostly due to the utilization of HVOF technology to apply the coating on the surface of the spike. The HVOF technology applied the powder SAM 2X5 composite on the surface of stainless-steel be melting the powder in a combustion chamber at temperatures that range from 2,200 to 3000 ^{o}C. This high operating temperature negatively affected the corrosion behavior of the SAM

2X5 composite because it increased the percent crystallinity along with the boundaries between the crystalline and amorphous phases which accelerated the effect of localized intergranular corrosion.

To determine the deterioration mechanism of the coating, cross sectional SEM images were taken of coated spikes throughout the 4-month monitoring period to calculate the average thickness of the coated layer. It was found that pre-installed samples had an average coating thickness of 92.37μm. After two months the thickness decreased to an average value of 67.66 μm and at four months, the coated layers was very thin with an average thickness of 29.17 μm. Additionally, SEM images of the coated surface revealed a highly porous layer which increased the water penetration rate and resulted in reducing the service life of the SAM-based coating.

Despite the unexpected rapid deterioration of the SAM-based coating, the Coronado Bridge application was a first attempt and another low temperature coating technology should be used to develop a high performance SAM-based coating. It is recommended to use physical vapor deposition sputtering process to develop the SAM-based coating because operating temperatures do not exceed 500 ^{o}C which will maintain the amorphous structure of the SAM 2X5 composite where it has the highest ability to resist corrosion.

Based on the results of the electrochemical and microstructural analysis of SAM coated stainless steel spikes, the following conclusions can be made about the Coronado Bridge application:

- Over the time period of four months, the corrosion rate of the SAM-based coating increased from a low value of 9.10 mpy to a high value of 25.93 mpy.
- The corrosion rate of the uncoated stainless steel was also measured during the monitoring period and maintained a semi-constant value that ranged from 28.93 mpy to 30.96 mpy.
- Based on the collected corrosion rate data, the performance of the coating was calculated by comparing it to the uncoated stainless steel samples.
- During the monitoring period, the performance of the coating rapidly decreased from 66.29% to 16.24% after four months of exposure to the salty bay environment.
- Cross sectional SEM images were used to study the deterioration mechanism of the coating and calculate the average thickness of the coating which started at 92.37 μm and decreased to 29.17 μm after four months.
- Surface SEM images of the coated layer revealed high porosity which accelerated the water penetration levels and resulted in decreasing the service life of the SAM-based coating.
- HVOF thermal coating technology used to apply the SAM-based coating to the stainless-steel surface operated at very high temperatures that ranged from 2,200 to 3,000 ^{o}C which negatively affected the corrosion behavior of the SAM 2X5 composite.

- Therefore, it is recommended to use the low temperature physical vapor deposition sputtering process when developing a metallic coating that is composed of the SAM 2X5 composite which will maintain its amorphous structure where it has the highest ability to resist corrosion.

The bullet points stated in this section summarize the results of studying the corrosion behavior of the SAM 2X5 composite in the form of solid sintered discs and as a metallic protective coating. In conclusion to the current study, it was found that exposing the SAM 2X5 composite to high temperatures introduces crystalline defects into its amorphous structure which results in negatively effecting its ability to resist corrosion.

Section 8. References

[1] “Metal in Construction.” *Designing Buildings*, 6 Mar. 2019, www.designingbuildings.co.uk/wiki/Metal_in_construction.

[2] “Aluminum.” *Periodic Table*, Royal Society of Chemistry, 2019.

[3] Woodford, Chris. *Iron and Steel*. Aug. 2018.

[4] Walters, Nicholas, and Bradley Forder. “World Steel in Figure 2019.” *World Steel Association,* 3 June 2019, www.worldsteel.org/media-centre/press-releases/2019/world-steel-in-figures-2019.html.

[5] Koch, Gerhardus, Varney, Jeff, Thompson, Neil, Moghissi, Oliver, Gould, Melissa and Prayer Joe. “International Measures of Prevention, Applications and Economics of Corrosion Technologies Study.” *NACE IMPACT International*, Mar. 2016, pp. 1–13.

[6] *Protective Coatings*. American Galvanizers Association, 2018, galvanizeit.org/corrosion/corrosion-protection/protective-coatings.

[7] *Paint.* American Galvanizers Association, 2018, galvanizeit.org/corrosion/corrosion-protection/protective-coatings/paint.

[8] *Powder*. American Galvanizer Association, 2018, galvanizeit.org/corrosion/corrosion-protection/protective-coatings/powder.

[9] Baxter, Richard, and Jim Britton. *Offshore Cathodic Protection 101: What It Is and How It Works.* Deepwater, 2013, www.cathodicprotection101.com/.

[10] “Passivation.” *Corrosion & Prevention Conference and Exhibition*, CorrosionPedia, Nov. 2018, www.corrosionpedia.com/definition/860/passivation.

[11] Zolotukhin, V, and Y Kalinin. “Amorphous Metallic Alloys.” *Soviet Physics Uspekhi*, vol. 33, Sept. 1990.

[12] Kelly, James P, Fuller, Seth M, Seo, Kyungah, Novitskaya, Ekaterina, Eliasson, Veronica, Hodge, Andrea M and Graeve, Olivia A. “Designing in Situ and Ex Situ Bulk Metallic Glass Composites via Spark Plasma Sintering in the Supper Cooled Liquid State.” *Materials and Design*, 23 Dec. 2015.

[13] “Amorphous Metals.” *Wikipedia*, June 2019.

[14] Graeve, Olivia. “Amorphous Solids.” Topics in Engineering. Lecture 14 of MATS 250, Oct. 2018, La Jolla, UCSD - Warren Lecture Hall.

[15] Abrosimova, Galina, and Alexandr Aronin. “Amorphous and Nanocrystalline Metallic Alloys.” *Institute of Solid State Physics*.

[16] Cai, Shengqiang. “Structure and Morphology.” MATS 257 - Polymer Science and Engineering. Lecture # 7, 24 Oct. 2018, La Jolla, UCSD Jacob School of Engineering.

[17] Aditya, A, Wu, H, Arora, H, and Mukherjee, S. “Amorphous Metallic Alloys: Pathways for Enhanced Wear and Corrosion Resistance.” *The Minerals, Metals & Materials Society,* vol. 69, May 2017, doi: 10.1007/s11837-017-2384-9.

[18] “High Velocity Oxygen Fuel (HVOF) Coating.” *Body Cote*, 2018, www.bodycote.com/services/surface-technology/high-velocity-oxygen-fuel-hvof-coating/.

[19] Li, M, and P Christofides. “Modeling and Control of High-Velocity Oxygen-Fuel (HVOF) Thermal Spray: A Tutorial Review.” *Journal of Thermal Spray Technology,* vol. 18, Dec. 2009, doi: 10.1007/s11666-009-9309-2.

[20] “High Velocity Oxygen Fuel Coating, HVOF.” *Manufacturing Guide*, 2017, www.manufacturingguide.com/en/high-velocity-oxygen-fuel-coating-hvof.

[21] “Coated Systems.” *Methu Group*, 2019, www.methugroup.com/en/products/rolls/systems.

[22] “Thermal Spray.” *Techno Service,* Techno Service Workshops, 2015, technoservice-me.com/home/workshop/.

[23] Macdonald, J.Ross. “Corrosion of Materials.” *Impedance Spectroscopy*, John Wiley & Sons, 1987, pp. 260–267.

[24] Kanoun, Olfa. *Lecture Notes on Impedance Spectroscopy*. CRC Press, 2011.

[25] Kain Escobar, and Laura A. Cantu. “Corrosion Basics.” *Chemistry - LibreTexts*, June 2019, chem.libretexts.org/Bookshelves/Analytical_Chemistry/Supplemental_Modules_(Analytical_Chemistry)/Electrochemistry/Exemplars/Corrosion/Corrosion_Basics.

[26] What is Corrosion? https://saylordotorg.github.io/text_general-chemistry-principles-patterns-and-applications-v1.0/s23-06-corrosion.html

[27] “Different Types of Metal Corrosion and Basic Preventative Coatings.” *Thomas Industry Update,* Thomas Publishing Company, 2019, www.thomasnet.com/articles/chemicals/corrosion-resistant-coatings.

[28] Fontana, and Green. “Eight Forms of Corrosion.” *NACE International,* National Society of Corrosion Engineers, 1967, nace.org/resources/general-resources/corrosion-basics/group-1/eight-forms-of-corrosion.

[29] “Different Types of Corrosion.” *PROTECH*, Oxyplast UK Limited, 2019, oxyplastuk.com/technical/different-types-of-corrosion/.

[30] National Association of Corrosion Engineers. “Intergranular Corrosion.” *NACE Resources*, NACE International, 2018, www.nace.org/resources/general-resources/corrosion-basics/group-2/intergranular-corrosion.

[31] “Basics of Electrochemical Impedance Spectroscopy.” *Gamry Instruments*, 2018, www.gamry.com/application-notes/EIS/basics-of-electrochemical-impedance-spectroscopy/.

[32] Bai, Rekha, and V K Pillai. “The Role of Reference and Counter Electrodes in a 3-Electrode System.” *Research Gate*, Indian Institute of Technology Delhi, Sept. 2013.

[33] Kissinger, and Bott. “Reference Electrodes.” *Chemistry | LibreTexts*, United States of America Department of Education, June 2019.

[34] “Calomel Electrode.” *Chemistry Glossary,* Eni Generalic, Oct. 2018, glossary.periodni.com/glossary.php?en=calomel electrode.

[35] “Silver/Silver Chloride Reference Electrode.” *Corrosion: Impact, Principles and Practical Solutions,* Corrosion Engineering, Aug. 2018, corrosion-doctors.org/Corrosion-Thermodynamics/Reference-Half-Cells-Silver.htm.

[36] “Working Electrode.” *Corrosion & Prevention Conference and Exhibition*, CorrosionPedia, 2018, www.corrosionpedia.com/definition/1184/working-electrode.

[37] Abul Hossain, Md, Abdul Gafur, M, Gulshan, F, and Kurny, A. “Electrochemical Investigation of the Corrosion Behavior of Heat Treated Al-6Si-0.5Mg-XCu (x =0, 0.5 and 1) Alloys.” *Research Gate,* Mar. 2015, www.researchgate.net/figure/Schematic-representation-of-the-three-electrode-system-cell_fig6_276911959.

[38] Holm, Thomas. “The Purpose of Electrolyte in a Galvanic Cell.” *Electrochemistry & Materials Science and Engineering*, Norwegian University of Science and Technology, Dec. 2018.

[39] “What Is a Potentiostat?” *CorrosionPedia*, 2017, www.corrosionpedia.com/definition/914/potentiostat.

[40] “Calculation of Corrosion Rate.” *Gamry Instruments*, 2018, www.gamry.com/Framework Help/HTML5 - Tripane - Audience A/Content/EFM/Introduction/Calculation of Corrosion Rate.htm.

[41] Loreto, Giovanni, Di Benedetti, Matteo, Nanni, Antonio and R. Iovino. “Evaluation of Corrosion Effect in Reinforced Concrete by Chloride Exposure.” *Research Gate*, The International Society for Optical Engineering, Mar. 2011.

[42] Helmenstine, Anne M. “Crystallization Definition.” *Thought Co*, May 2019, www.thoughtco.com/definition-of-crystallize-605854.

[43] Miray Çelikbilek, Ali Erçin Ersundu and Süheyla Aydın. “Crystallization Kinetics of Amorphous Materials.” *Istanbul Technical University*, Crystallization Processes, Apr. 2012.

[44] “The Solid State of Crystalline and Amorphpus Solids.” *Toppr Chemistry Guides*, June 2015, www.toppr.com/guides/chemistry/the-solid-state/crystalline-and-amorphous-solids/.

[45] Montgomery, Jordan. “Mechanical Properties of Materials.” *ASM Materials Education Foundation*, The Materials International Society, 2016.

[46] “How to Avoid Intergranular corrosion?” *Heat Exchangers Technical Documentation,* SACOME, Sept. 6AD, 2017, www.sacome.com/en/avoid-intergranular-corrosion/.

[47] Lawrynowicz, Z. “Effect of the Degree of Cold Work and Sensitization Time on Intergranular Corrosion Behavior in Austenitic Stainless Steel.” *Advances in Materials Science*, vol. 19, Mar. 2019, doi: 10.2478.

[48] Basu, Bikramjit. “Some Fundamentals on Spark Plasma Sintering as a Processing Tool to Fabricate Biomaterials.” Department of Materials Science and Engineering. Indian Institute of Technology Kanpur, Indian Institute of Technology Kanpur.

[49] “Spark Plasma Sintering.” *Wikipedia*, Feb. 2019.

[50] Reed, Corey. “Sintering; Densification vs. Coarsening.”, June. 2016.

[51] Li, X, Yang, C, Lu, H, Luo, X, Li, Y, and Ivasishin, O. “Correlation between Atomic Diffusivity and Densification Mechanism during Spark Plasma Sintering of Titanium Alloy Powders.” *Journal of Alloys and Compounds,* vol. 787, 30 May 2019, pp. 112–122., doi: 2019.02.002.

[52] Dewitt, Darren. “Operating Spark Plasma Sintering Instrument.” SPS Training Session. SPS Training Session, Mar. 2019, La Jolla, UCSD - Mechanical & Aerospace Engineering Labs.

[53] Rawlings, Brandon. “Crystallinity in Polymers.” *University of Texas at Austin*, Feb. 2009, pp. 9–19.

[54] Lange's Handbook. “Standard Heats and Free Energies of Formation and Absolute Entropies of Elements and Inorganic Compounds.” *Wired Chemist*, Lange's Handbook, 2019.

[55] Christopher Muscato. “Coronado Bridge: History, Construction & Facts.” *Architectural Structures*, Study. Com, 2015, study.com/academy/lesson/coronado-bridge-history-construction-facts.html.

[56] Matt Boone. “Suicide Prevention Spikes Installed along Coronado Bridge.” *Local News*, ABC 10 News - San Diego, Feb. 2019, www.10news.com/news/local-news/san-diego-news/suicide-prevention-spikes-installed-along-coronado-bridge.

[57] “Percentage Change | Increase and Decrease.” *Skills You Need*, www.skillsyouneed.com/num/percent-change.html.

[58] Hughes, Matt. “What Is Physical Vapor Deposition Coating?” *Semicore*, Semicore Equipment, Aug. 2018.

[59] “What If PVD Sputtering.” *YouTube,* Semicore Equipment, Nov. 2013.

[60] Lagoski, Thomas J, Coutu A, Ronald and Starman A, Lavern. “Retroreflector for Photonic Doppler Velocimetry.” *Research Gate*, International Society for Optical Engineering, Aug. 2009.

[61] “What Is Thermal Evaporation.” *ALB Materials*, 2019.

[62] “Mechanism of Vacuum Thin Film Coating System.” *ShinMaywa Industries,* ShinMaywa Worldwide, 2017.